TECHNICAL UNIVERSITY OF CRETE
ELECTRICAL AND COMPUTER ENGINEERING DEPARTMENT
TELECOMMUNICATIONS DIVISION

Environmental Scatter Radio Sensors with RF Energy Harvesting

by

Spyridon-Nektarios Daskalakis

A THESIS SUBMITTED IN PARTIAL FULFILLMENT OF
THE REQUIREMENTS FOR THE MASTER OF SCIENCE OF

ELECTRICAL AND COMPUTER ENGINEERING

July 20, 2016

THESIS COMMITTEE

Associate Professor, Aggelos Bletsas, *Thesis Supervisor*
Associate Professor, Eftichios Koutroulis
Associate Professor, Matthias Bucher

Abstract

Real-time monitoring of environmental parameters, such as soil moisture, with wireless sensor networks (WSN), is invaluable for precision agriculture. However, conventional radios in large-scale deployments are limited by power consumption, cost and complexity constraints. Scatter-radio, a promising technology, allows the development of large-scale and low-cost WSN. In this work, the development of an analog scatter-radio WSN for soil moisture is presented. The WSN consists of low-cost (6 Euro per sensor), low-power (in the order of 200 μW per sensor) soil moisture scatter radio sensors, with high communication range (up to 250 m). The WSN utilizes analog frequency modulation (FM) in a bistatic network architecture, while the sensors operate simultaneously, using frequency division multiple access (FDMA). The network utilizes an ultra-low cost software-defined radio reader and proposes a custom microstrip capacitive sensor with a simple calibration methodology. Overall root mean squared error (RMSE) below 1% is observed, even for ranges of 250 m. In order to supply the sensor with energy, a radio frequency (RF) energy harvesting supply system is also presented. The system collects the unused ambient RF energy from scatter radio emitters and from one FM station. The design consists of a double diode rectifier with operation in the two frequencies of 900 MHz and 97.5 MHz, simultaneously, utilizing a low-cost, lossy FR-4 substrate and a low-complexity rectifier circuit. The achieved RF-to-DC rectification efficiency was 14.49% and 27.44% at 868 MHz and 97.5 MHz, respectively, and 20 dBm input power. The rectifier was connected to a commercial boost converter in order to manage and improve the output power of the rectifier. Finally, the end-to-end efficiency of the system was 21%, at 97.5 MHz and 15 dBm input power. This work offers a concrete example of ultra-low power and cost wireless sensor networking with (unconventional) novel scatter radio technology.

This work was supported by the ERC04-BLASE project, executed in the context of the "Education & Lifelong Learning" Operational Program of the National Strategic Reference Framework (NSRF), General Secretariat for Research & Technology (GSRT), funded through European Union-European Social Fund and Greek national funds. It was also supported by Onassis Foundation graduate studies 2015/16 scholarship and by the COST Action IC1301 WiPE Wireless Power Transmission for Sustainable Electronics.

Thesis Supervisor: Associate Professor Aggelos Bletsas

Acknowledgements

I would like to thank my family and my friends for the invaluable moral support they provided. My parents, deserve mention, although I couldn't possibly write enough. I would also like to thank all members of Technical Univ. of Crete, school of ECE Fab/Telecom Lab and especially my advisor and mentor Aggelos Bletsas, who has offered me all the guidance I needed and facilitated my academic growth, throughout my course as a graduate student. Moreover, special thanks to Dr. Stylianos D. Assimonis who introduced me to the world of electromagnetism and energy harvesting. Finally I would like to thank Alexander S. Onassis Public Benefit Foundation for the 2015/16 scholarship program during my MSc studies.

Table of Contents

List of Figures

List of Tables

Chapter 1

Introduction

Nowadays, modern agriculture applications necessitate cheap, effective, low maintenance and low-cost wireless telemetry for various environmental parameters [1], such as environmental humidity, soil moisture, barometric pressure and air/leaf stomata temperature [2–5]. Continuous and dense environmental monitoring is critical for optimal crop and water management techniques and thus, wireless sensor network (WSN) technologies for microclimate monitoring in extended areas, are indispensable within this topic [1]. One important environmental variable that needs careful monitoring, especially in agriculture and water management applications, is percentage soil moisture (%SM). Prior art has offered novel soil moisture capacitive sensors integrated with discrete wireless radio module [6], [7] or discrete processing chip [8], including ink-jet fabrication designs.

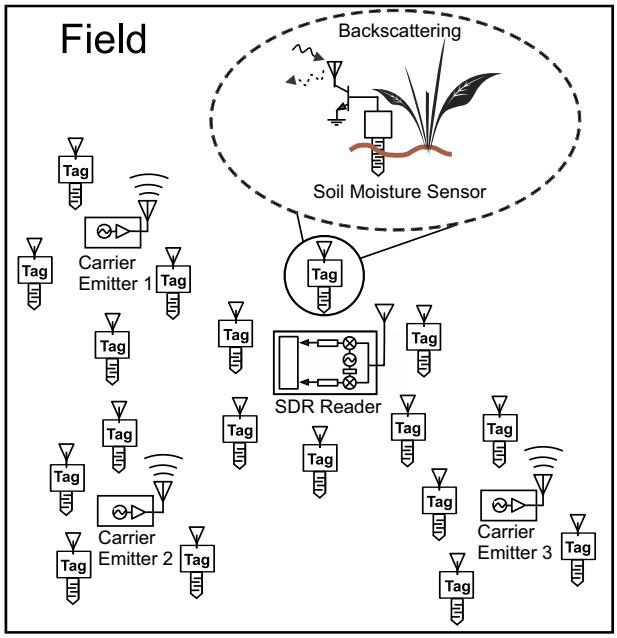

Figure 1.1: Bistatic soil moisture scatter radio WSN. There could be multiple carrier emitters and one software-defined radio (SDR) reader.

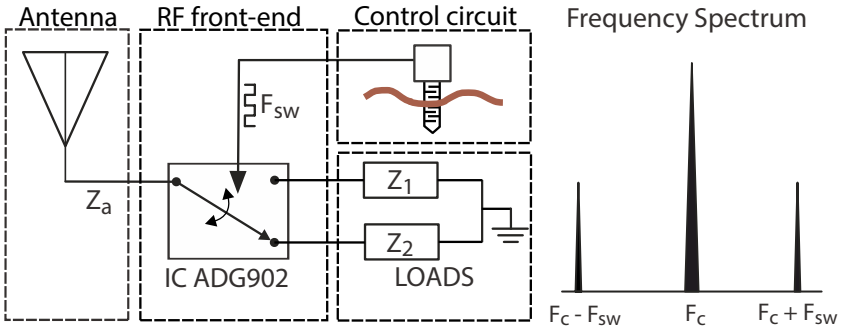

Figure 1.2: Scatter radio principles: The low power RF switch "ADG902" alternates the termination loads Z_1 and Z_2 of the antenna (corresponding to reflection coefficients Γ_1, Γ_2, respectively) with frequency F_{sw}. When the illuminating carrier frequency is F_{c}, two new subcarrier frequencies $F_{\text{c}} \pm F_{\text{sw}}$ appear in the spectrum. Difference $|\Gamma_1 - \Gamma_2|$ should be maximized; however, practical constraints (e.g., parasitics) restrict such maximization.

Conventional WSNs consist of a network of nodes (possibly in a mesh architecture), transferring monitored environmental data to a base station. Each node typically employs a Marconi-type radio (e.g. ZigBee/Lora-type), controlled by a microcontroller unit (MCU) and the sensors. However, large-scale deployments of conventional WSN technology are uncommon, due to power consumption, installation and maintenance cost. Work in [9] is one rare case of large-scale, outdoor demonstration, with packaging/long-term deployment cost per wireless sensor in the order of 50 Euro.

In order to address power consumption and cost per sensor constraints, scatter radio has recently attracted interest for wireless sensing development (Fig. 1.1). In the first work for scatter radio networking [10], it is showed that, using scatter radio, the front end of each sensor is simplified to a reflector that modulates information on the sensor's antenna-load reflection coefficient; in scatter radio, communication is performed by means of reflection, where signal conditioning such as filtering, mixing or amplification at the sensor/tag are typically avoided; in that way, low power consumption is needed, offering opportunities for battery-less operation [11, 12], e.g., each sensor can be powered using ambient radio frequency (RF) energy with appropriate rectifiers (e.g., [13–15]) or using multiple kinds of ambient energy sources, such as RF and solar energy, simultaneously (e.g., [16]).

A RF rectifier example is presented below, in this work. Sensor designs with scatter radio typically exploit variations of sensor's antenna properties [17], based on the environmental parameter under monitoring, such as the (mechanical) shape (e.g., [18]) or the dielectric constant (e.g., [19]); chip-less designs typically include appropriately-designed antenna loads with delay lines (e.g., work in [20] and references therein); another way to construct scatter radio signal reflectors is by using a switch, connecting sensor's antenna to different loads. Elevating the above principles from sensing to networking of several, simultaneously operating, scatter radio sensors is not trivial and emerges as a challenging topic of research.

Work in [21] offered frequency-modulated scatter radio signals with soil moisture information and duty-cycled operation that reduced the operating bandwidth, while experimental results were reported for only two sensors and commodity software defined radio (with cost in the order of 1000 Euro). The tag-to-reader communication range was in the order of 100 meter. In this work, 50% duty-cycle of frequency modulated soil moisture is achieved with a new circuit, which also reduces the overall power consumption; 50% duty cycle is crucial for getting rid of even-order harmonics and thus, enhancing the available bandwidth for multiple scatter radio sensors simultaneous access [22]. Moreover, this work offers different and more accurate sensor calibration, experimental results for multiple sensors, ranges in the order of 250 meter with ultra-low cost, portable SDR (that costs 7 Euro), while scalability issues are further examined.

1.1 Scatter Radio Principles

Scatter radio communication, known from 1948 [23], is currently exploited in the radio frequency identification (RFID) industry. Communication is implemented with an antenna, a control circuit and a radio frequency (RF) switch between them. The switch alternatively terminates the tag/sensor antenna between (usually two) loads Z_1 and Z_2 (Fig. 1.2). The control circuit is responsible for the modulation operation. Tag/sensor antenna S_{11} parameter (i.e., reflection coefficient Γ), associated with each antenna terminating load, is modified when the antenna load is changed. The different termination loads offer different reflection coefficients, (Γ_1

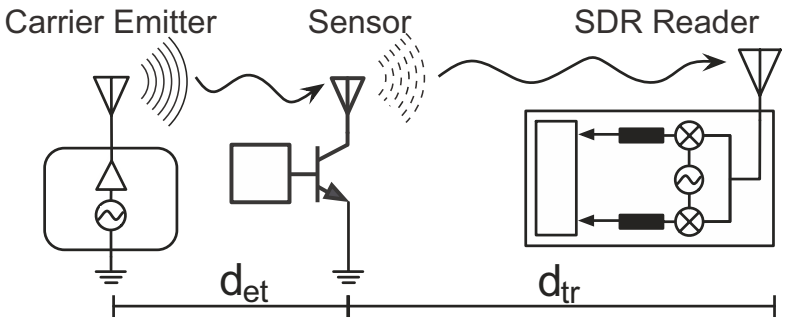

Figure 1.3: Bistatic topology of a scatter radio link; emitter produces the carrier signal which is modulated by sensor nodes and finally, the reflected signal is received by a software defined radio (SDR) reader. d_{et} and d_{tr} denote emitter-to-tag and tag-to-reader distance, respectively. Notice that in this work, one emitter illuminates multiple tags, simultaneously.

and Γ_2) according to the following [24–28]:

$$\Gamma_{\mathrm{i}} = \frac{Z_{\mathrm{i}} - Z_{\mathrm{a}}^{*}}{Z_{\mathrm{i}} + Z_{\mathrm{a}}}, \tag{1.1}$$

with $\mathrm{i} = 1, 2$ and Z_{a} denoting the antenna impedance. Therefore, amplitude and phase of the carrier signal - induced at the sensor antenna -are modulated and the signal is reflected (scattered) back towards a receiver. As a result, when a continuous wave (CW) with frequency F_{c} is incident on the sensor antenna, which is alternatively terminated between two loads at a rate F_{sw}, two new subcarrier frequencies appear in the spectrum (Fig. 1.2); their frequency values are given by [10]:

$$F_{\mathrm{sub},1} = F_{\mathrm{c}} + F_{\mathrm{sw}}, \tag{1.2}$$

$$F_{\mathrm{sub},2} = F_{\mathrm{c}} - F_{\mathrm{sw}}. \tag{1.3}$$

While scatter-radio principles have been restricted to communication ranges of up to a few meter [29–31], a novel scatter radio sensor network (WSN) for relative humidity (%RH) measurements was presented in [32]. That WSN consisted of low-power and low-cost analog designs of wireless transmitters sensor nodes/tags

[1] with scatter radio and extended communication ranges. Each tag employed bistatic semi-passive scatter radio principles [33], [34]. In order to address the small communication range problem, the WSN utilized the bistatic topology (where the carrier emitter was placed in a different location from the reader) and semi-passive (i.e., battery-assisted) tags. The utilization of the bistatic topology is illustrated in Fig. 1.3. Using the above concepts, it was shown possible to implement large-scale networks, comprising of low-cost sensor/tags, a few emitters operating at the European RFID band ($865 - 868$ MHz) [35] and a single software-defined radio (SDR) receiver, detecting the backscattered signals.

The first part of this work describes the development of a bistatic scatter radio WSN, that measures soil moisture percentage (%SM) with analog, frequency modulation (FM) principles and ranges in the order of 250 meter. In sharp contrast to prior art, this work offers a) custom capacitive sensing, b) soil moisture sensing and networking of multiple sensors (with corroborating experimental results), c) reception with ultra-low cost software-defined radio (SDR) that costs only a few Euro and d) special modulation design that offers scatter radio modulation signals with 50% duty cycle; the latter will be shown to be important for signal-to-noise ratio improvements at the SDR receiver, as well as for network scalability purposes. In second part, a RF energy harvesting system for sensor power supply is presented. The system uses RF energy from scatter radio emitters and one FM station in order to collect the unused ambient energy.

For the first part, Section 2.1 offers the design and implementation of the scatter radio sensor circuit, multiple access capability and power consumption tradeoff. Section 2.5 offers the SDR receiver design, based on a 8-bit ultra-low cost SDR, Section 2.6 describes the simple calibration procedure and Section 2.7 offers the experimental results, including a relevant network demonstration and bistatic range measurements. The second part is summarized as follows: in Section 3.1, a rectifier circuit is presented. In Section 3.2, a dual band printed antenna is described. In Section 3.3, the use of a commercial DC-DC converter is described and the overall end-to-end efficiency is derived. Finally, overall work is concluded in Chapter 4.

[1] In line with standard RFID terminology, the terms "tag","node" or "sensor node" will be used interchangeably.

Chapter 2

Sensors Design and Implementation

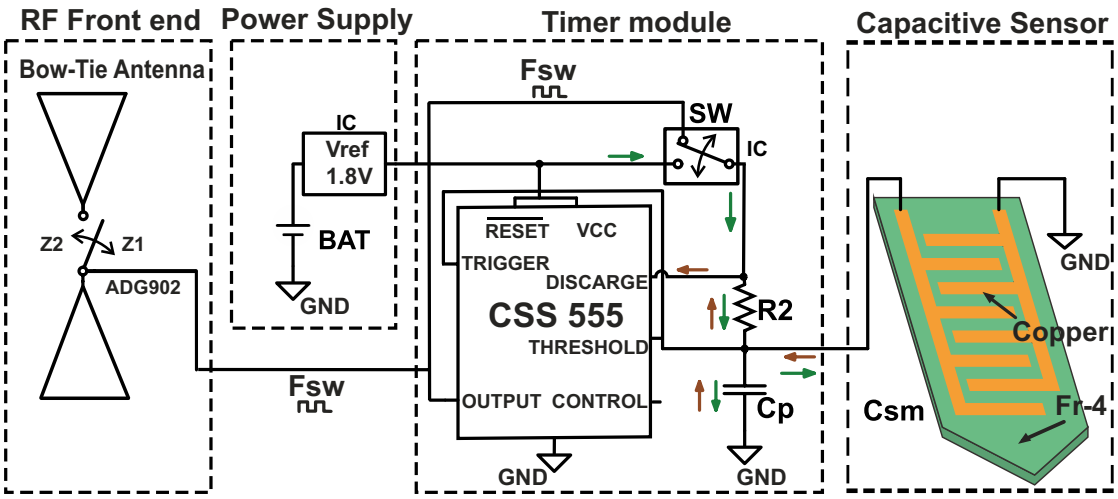

Figure 2.1: The analog backscatter sensor node schematic. Each node consists of the capacitive soil moisture sensor to be inserted in the soil, the timer module that converts the variable capacitance to frequency (C2F) and the scatter radio front end. The variable frequency signal controls the antenna RF switch. The node is supplied by a voltage reference circuit.

The design target of the tags is to produce voltage pulses of fundamental frequency that depends on the %SM value and control the rate with which the antenna termination loads are alternated. For this purpose, the circuit diagram of Fig. 2.1 was designed, consisting of a custom capacitive soil moisture sensor, the capacitance-to-frequency converter (C2F), the power supply circuit and the scatter radio front-end.

2.1 Sensor & C2F Converter

A single astable multi-vibrator circuit with "555" timer functioned as the capacitance-to-frequency converter. The timer was the ultra low power monolithic CSS555 [36] with minimum current consumption of 5 uA at 1.2 V. The timer was connected to a resistor-capacitor network of R_2, C_p and to the custom, microstrip capacitive sensor C_sm (Fig. 2.1). The capacitive sensor consisted of two isolated conductive plates, separated by a narrow gap, on low cost FR-4 substrate with thickness 1.5 mm and and dielectric constant $\epsilon_\mathrm{r} = 4.6$; waterproofness was facilitated using the green solder mask as insulation. The followed capacitance sensor design is equivalent to a number of co-planar plate capacitors, inserted in parallel into the soil, which alters the dielectric constant; if soil is moist (high %SM), the capacitor will contain more water, resulting to higher capacitance (i.e., high C_sm), while dry soil offers lower capacitance. More informations about the sensor design and simulations are available below 2.1.2.

The fundamental frequency F_sw of the pulse depends on the resistor and the capacitor, connected to the TRIGGER and THRESHOLD pins of the "555" timer. As depicted in Fig. 2.1 (arrows), the parallel capacitors (C_p and C_sm) are periodically charged (green arrows) and discharged (brown arrows) through R_2 and an electronic, single-pole single-throw (SPST) switch (SW). The SW is open when timer output is in logic "low", so there is no leakage current through the SW loop and has been placed in order to reduce consumption, while attaining pulses with duty cycle of 50%; the latter is a fundamental difference compared to other capacitance-to-frequency converters in the literature (e.g., [32]). The timer output square wave pulse is offered with fundamental frequency given by:

$$F_\mathrm{sw} = \frac{1}{2\ln(2)R_2(C_\mathrm{p} + C_\mathrm{sm})}. \tag{2.1}$$

According to [37], the power of the fundamental subcarrier frequency of the scattered signal is given by:

$$P(a) = \left[\frac{A\sqrt{2}}{\pi}\sin(\pi D)\right]^2, \tag{2.2}$$

where A is the peak-to-peak amplitude of the pulse signal and D is the duty cycle; thus, the backscattered signal power will be increased when D approaches the value of 50%. Using a single analog switch (SW in Fig. 2.1) and only one resistor (R_2) in the typical astable multi-vibrator circuit, the duty cycle of the produced pulse is calculated as follows:

$$D = \frac{R_2}{2R_2} = 50\%. \tag{2.3}$$

The capitulation procedure is explained in the next subsection 2.1.1. According to its Fourier series analysis, a 50% duty-cycle square pulse consists of odd order harmonics of the fundamental frequency, i.e., even order harmonics are not present. Therefore, square waves without 50% duty-cycle occupy additional bandwidth, limiting the capacity of the designed network in a specific frequency band.

2.1.1 50% Duty Cycle Circuit Analysis

If the overall capacitance is denoted as $C = C_{\mathrm{p}} + C_{\mathrm{sm}}$, the time, during which the C is charged from $1/3V_{\mathrm{CC}}$ to $2/3V_{\mathrm{CC}}$, is equal to the time that the output is high. The time is denoted as T_{HIGH}. Voltage across C at any instant during charging period is given as,

$$V_{cap} = V_{\mathrm{CC}}(1 - e^{\frac{t}{R \times C}}). \tag{2.4}$$

Time t_1 when C is charged from 0 to $1/3V_{\mathrm{CC}}$, is calculated from:

$$\frac{1}{3}V_{\mathrm{CC}} = V_{\mathrm{CC}}(1 - e^{-\frac{t_1}{R \times C}}), \tag{2.5}$$

$$t_1 = R \times C \times ln\frac{2}{3} = 0.405R \times C. \tag{2.6}$$

Time t_2 when C is charged from 0 to $2/3V_{\mathrm{CC}}$ is calculated from:

$$\frac{2}{3}V_{\mathrm{CC}} = V_{\mathrm{CC}}(1 - e^{-\frac{t_2}{R \times C}}), \tag{2.7}$$

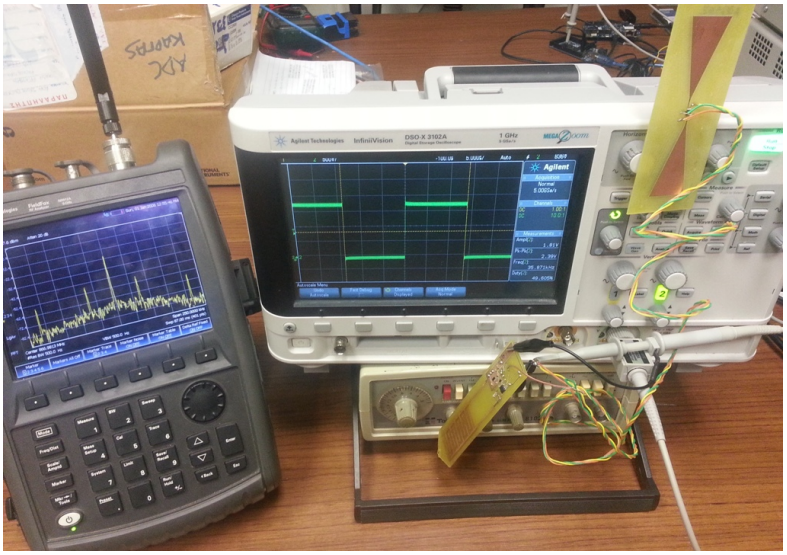

Figure 2.2: The output of sensor node is displayed on oscilloscope and its scattered signal (subcarrier) is displayed on spectrum analyser. For the backscatter communication was used a 868 MHz single carrier emitter.

$$t_2 = R \times C \times ln\frac{1}{3} = 1.0986R \times C. \tag{2.8}$$

So the time T_{HIGH}, when the capacitor is charged from $1/3V_{\text{CC}}$ to $2/3V_{\text{CC}}$ is taken by:

$$T_{\text{HIGH}} = (t_2 - t_1) = (1.0986 - 0.405)R \times C = 0.693R \times C. \tag{2.9}$$

If $R = R_2$,

$$T_{HIGH} = 0.693R_2 \times C \tag{2.10}$$

with R_2 is in Ohm and C in F. The time, when the capacitor is discharged from $1/3V_{\text{CC}}$ to $2/3V_{\text{CC}}$, is equal to the time that the output is low. Time is given as T_{L0W}. Voltage across the capacitor at any instant during discharging period is given as:

$$V_d = \frac{2}{3}V_{\text{CC}} \times e^{-\frac{t}{R_2 \times C}}. \tag{2.11}$$

Substituting $Vd = 1/3V_{\mathrm{CC}}$ and $t = T_{L0W}$ in above equation,

$$T_{LOW} = 0.693R_2 \times C. \tag{2.12}$$

Overall period of oscillation is,

$$T_{sw} = T_{\mathrm{HIGH}} + T_{\mathrm{LOW}} = 0.693 \times 2R_2 \times C. \tag{2.13}$$

The frequency of oscillation being the reciprocal of the overall period of oscillation T_{sw} is given as:

$$F_{sw} = \frac{1}{T_{sw}} = \frac{1.44}{2R_2 \times C}. \tag{2.14}$$

Equation indicates that the frequency of oscillation is independent of the supply voltage V_{CC}. Often the term duty cycle (D) is used in conjunction with the astable multivibrator circuit. The duty cycle, the ratio of the time t_c during which the output is high to the total time period T_{sw} is given as:

$$D = \frac{t_c}{T_{sw}} \times 100 = \frac{R_2}{2R_2} \times 100 = 50\%. \tag{2.15}$$

In Fig. 2.2 is obvious that the duty cycle of a tag is 50% and the F_{sw} is 35.9 kHz. In spectrum analyser is depicted that, there aren't even order harmonics, there is only the carrier (868 MHz) and odd order harmonics.

2.1.2 Capacitive Sensor Design and Simulations

The sensor consists of two isolated conductive plates, separated by a narrow gap. The assembly must be waterproof, as it will be in contact with moist soil for extended periods of time. As luck would have it, there is an inexpensive technology that enables us to build isolated conductors in arbitrary shapes with ridiculously small tolerances. This technology is printed circuit board fabrication with solder mask.

This work presents two different capacitive sensor designs. For the first, was designed a custom printed circuit board (PCB) that contains a number of co-planar

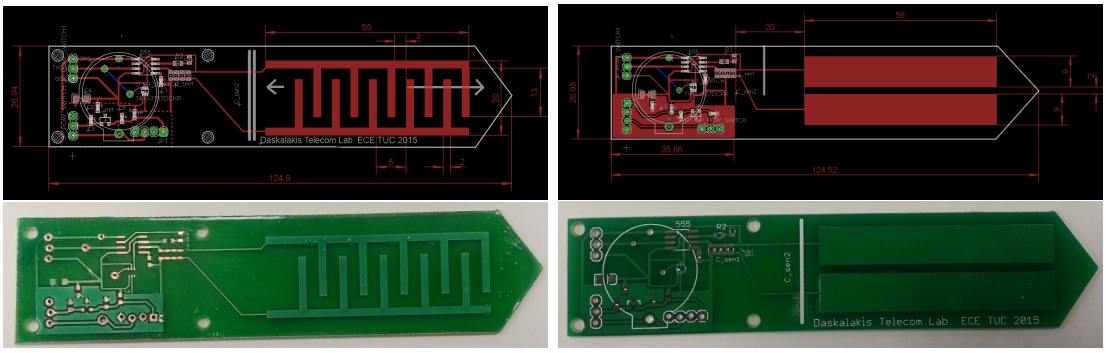

Figure 2.3: Eagle designs of tags. Intedigatated capacitive sensor (Up, Left) and parallel Plate capacitive sensor (Up, Right). Printed sircuit boards (PCBs) with solder mask (Down).

plate capacitors in parallel, called "interdigitated" (Fig. 2.3, left). Capacitance sums in parallel, so this will lead to a larger capacity of the entire assembly and therefore a larger capacity swing when the dielectric changes. For the second design, called "parallel plates" (Fig. 2.3, right), there are two parallel plates and a small gap between them. For both of them, there is the necessity to be measured the dielectric constant (ϵ_r) of the surrounding medium, and not of the PCB FR-4 fibreglass. In Fig. 2.3 are depicted the sensors as designed in Eagle software. The entire tag is about 125 mm long and 27 mm wide. Sensors dimensions are about 55 mm long and 20 mm wide. On the reverse side of the PCB there are not traces of sensor. All PCBs sport a pointy tip for easy insertion into soil. Note the relatively large gap (2-3 mm) between the plates. The capacity is actually inversely proportional to the gap.

The sensors, covered by solder mask, were simulated and measured. Results was useful for the WSN design. For the simulations was used the Advanced Design System (ADS) by Agilent. Microwave analysis was performed in order to estimate the capacitance. Two cases of simulation were investigated: initial, the capacitors was surrounded by air (air-case) and next by water (water-case). Two models of the sensor ("interdigitated" and "parallel plates") were designed in ADS with same dimensions as Eagle designs. Above FR-4 substrate, a water proof layer (green solder mask) was added with thickness 75 μm, $\epsilon_r = 3.56$ and $tan\delta = 0.038$. Water proof material, and FR-4 was surrounded by air ($\epsilon_r = 1$, thickness 100 mm) and water ($\epsilon_r = 78.2$, $tan\delta = 0.4$ and thickness 100 mm) for air-case and water-case,

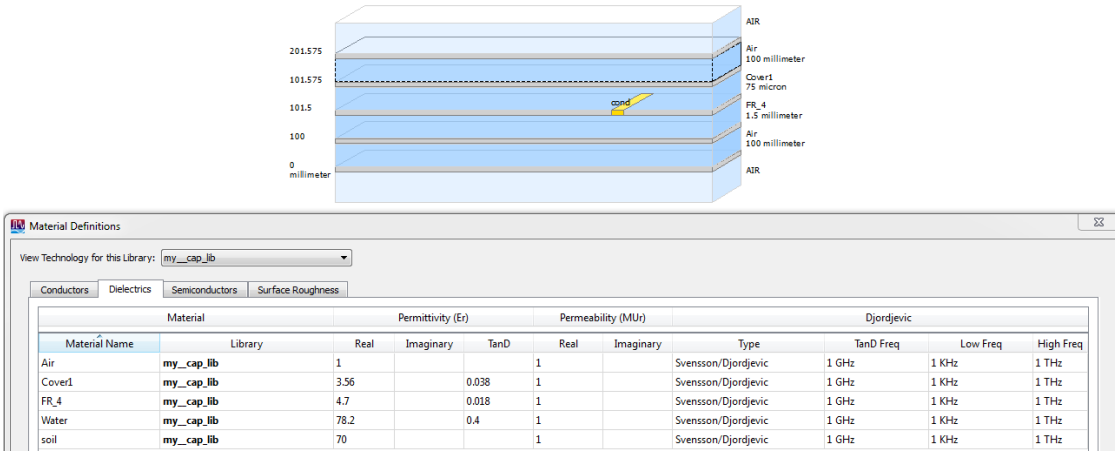

Material		Permittivity (Er)			Permeability (MUr)		Djordjevic			
Material Name	Library	Real	Imaginary	TanD	Real	Imaginary	Type	TanD Freq	Low Freq	High Freq
Air	my_cap_lib	1			1		Svensson/Djordjevic	1 GHz	1 KHz	1 THz
Cover1	my_cap_lib	3.56		0.038	1		Svensson/Djordjevic	1 GHz	1 KHz	1 THz
FR_4	my_cap_lib	4.7		0.018	1		Svensson/Djordjevic	1 GHz	1 KHz	1 THz
Water	my_cap_lib	78.2		0.4	1		Svensson/Djordjevic	1 GHz	1 KHz	1 THz
soil	my_cap_lib	70			1		Svensson/Djordjevic	1 GHz	1 KHz	1 THz

Figure 2.4: ADS material definition preview.

respectively. The materials list is depicted in Fig. 2.4. Scattering (S) parameters analysis was performed at frequency range from 100 kHz to 300 kHz and effective capacitance C, in pF was calculated according to:

$$C = \frac{-\mathrm{e}^{12}}{2\pi F * \Im(\frac{1}{Y_{1,1}})}, \tag{2.16}$$

with $Y_{1,1}$, the first element of admittance matrix (Y parameters). The capacitance results of water-case are depicted in Fig. 2.5. Also the control circuit of sensor was modelled and simulated only in air-case. The control circuit is connected with the sensor in the same PCB and effects the soil moisture sensor with a fixed capacitance of 1.5 pF.

After the simulations, sensors were measured with a inductance, capacitance, resistance (LCR) meter. The LCR meter was calibrated on five different frequencies (100, 110, 150, 200 and 300 kHz) and measurements in pF are depicted in Tables 2.1 and 2.2. Measurements were separated in two cases, in the first case, sensors were measured in the air (Air Meas) and in the second case, the sensors were sunk in a glass of water (Water Meas). Tables also shows the results from simulations in pF, estimated at 100, 110, 150, 200 and 300 kHz. It is obvious that the control circuit capacitance has been added in simulations. A good agreement between simulation and measurement results is observed for “interdigitated” sen-

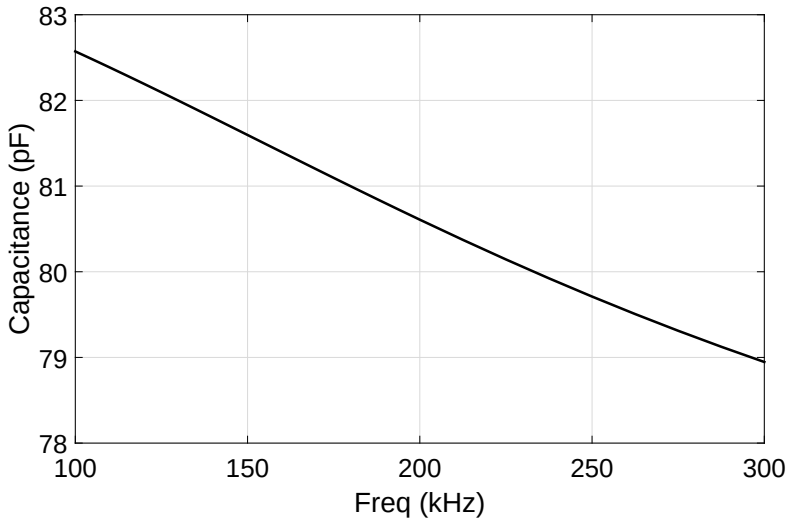

Figure 2.5: Soil moisture sensor capacitance versus frequency. ADS simulation for water case.

Table 2.1: "Interdigitated" sensor measurement and simulation data in (pF).

Case	100 kHz	110 kHz	150 kHz	200 kHz	300 kHz
Air Meas 1	4.36	4.37	4.36	4.34	4.32
Air Meas 2	5.3	5.4	5.37	5.28	5.24
Water Meas 1	83.62	83.8	80.61	78.51	75
Water Meas 2	78.18	77.21	75.78	74.45	72.8
Air Sim	–	$0.75 + 1.5$	$2.34 + 1.5$	$3.1 + 1.5$	$3.7 + 1.5$
Water Sim	$82.5 + 1.5$	$82.3 + 1.5$	$81.5 + 1.5$	$80.6 + 1.5$	$78.9 + 1.5$

sor but not for "parallel plates" sensor. For the "parallel plates", ADS is not able to manage the dynamic lines that extend to infinite. For the final tag design, the "interdigitated" sensor was selected due its smaller capacitance in the water.

2.2 Scatter Radio Antenna/Front-end

The scatter radio front-end of each tag (Fig. 2.6, right bottom) consists of a microstrip bow-tie antenna on low-cost FR-4 substrate with an embedded RF switch; the latter is the Analog Devices ADG902 [38], set up as SPST switch. The ADG902 was chosen due to its low insertion loss (0.8 dB at 1 GHz) and high isolation (43

Table 2.2: "Parallel plates" sensor measurement and simulation data in pF.

Case	100 kHz	110 kHz	150 kHz	200 kHz	300 kHz
Air Meas	5.78	5.85	5.79	5.8	5.77
Water Meas	554.7	544	505	445	370
Air Sim	–	–	$1.4 + 1.5$	$1.88 + 1.5$	$2.2 + 1.5$
Water Sim	$88 + 1.5$	$87.8 + 1.5$	$86.8 + 1.5$	$85.5 + 1.5$	$83.4 + 1.5$

dB at 1 GHz). The front-end design was tuned around 868 MHz, according to the maximization principles in [28].

With the significant assistance of Dr. Stylianos D. Asimonis, a bowtie antenna for each sensor design was adopted, due to its omnidirectional attributes (at the vertical to its axe level) and the ease of fabrication, with nominal gain of $G = 1.8$ dBi. Fig. 2.6 offers dimensions. Such antenna is appropriate for the bistatic scatter radio topology, while a different printed antenna with higher gain could increase the ranging distance in the bistatic topology; however appropriate alignment during installation could be needed in that case.

Five different scatter radio front-ends was designed and tested in this work. Two conventional designs were constructed (the RF switch PCB was separated from the antenna) with BF1118 and ADG919 RF switch. Also three novel designs (custom, coplanar bow tie antenna with the embedded RF switch in the same PCB) were constructed with BF1118, ADG919, and ADG902, RF switch. In order to be measured the performance, bi-static topology was used and spectrum analyser was the reader. The average captured power was measured after 500 iterations. The distance emitter-to-tag and tag-to-reader was 3 m and 9 m, respectively and the measurement took place into the ECE building. Switchers with better insertion loss and high isolation (ADG902 and ADG919), embedded on novel designs, had the better performance. As the final selection, was used the ADG902 due to its smaller cost.

2.3 Multiple Access

Simultaneous, collision-free operation of multiple, receiver-less sensors is facilitated with frequency-division multiple access principles [22], [10], [32]; every tag is as-

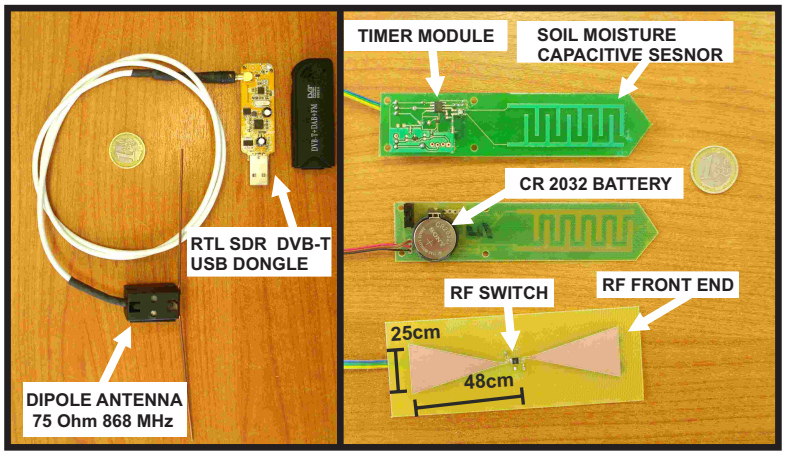

Figure 2.6: The fabricated sensor node (right). The green solder mask has been used as sensor insulation. Capacitive sensor and antenna/scatter radio front-end are fabricated on low-cost FR-4 substrate. The Realtek RTL software-defined radio (SDR) reader, depicted on the (left), is ultra-low cost on the order of 7 Euro.

signed a distinct frequency band (bandwidth), within which the switching rate (i.e., subcarrier frequency) of each tag's antenna load can vary. Fig. 2.7 illustrates the concept with both conceptual and experimental data.

Let $F^{\mathrm{L}}_{\mathrm{sw,i}}$ and $F^{\mathrm{H}}_{\mathrm{sw,i}}$ denote the subcarrier frequency output of the i-th tag for lowest and highest frequency, produced by the C2F converter when the %SM is 100 and 0, respectively. The required bandwidth B_{i} depends on the above two frequencies and is calculated as:

$$B_{\mathrm{i}} = F^{\mathrm{H}}_{\mathrm{sw,i}} - F^{\mathrm{L}}_{\mathrm{sw,i}}. \tag{2.17}$$

Assuming that C_{L}, C_{H} are the C_{sm} sensor capacitance for 0%, 100% SM, respectively, the $C_{\mathrm{p,i}}$ and $R_{2,\mathrm{i}}$ components of i-th tag are calculated according to (2.1), (2.17) as:

$$C_{\mathrm{p,i}} = \frac{-B_{\mathrm{i}}\, C_{\mathrm{L}} + F^{\mathrm{L}}_{\mathrm{sw,i}}\, (C_{\mathrm{H}} - C_{\mathrm{L}})}{B_{\mathrm{i}}}, \tag{2.18}$$

$$R_{2,\mathrm{i}} = \frac{B_{\mathrm{i}}}{2\ln(2)\; F^{\mathrm{L}}_{\mathrm{sw,i}}\; (C_{\mathrm{H}} - C_{\mathrm{L}})\; (F^{\mathrm{L}}_{\mathrm{sw,i}} + B_{\mathrm{i}})}. \tag{2.19}$$

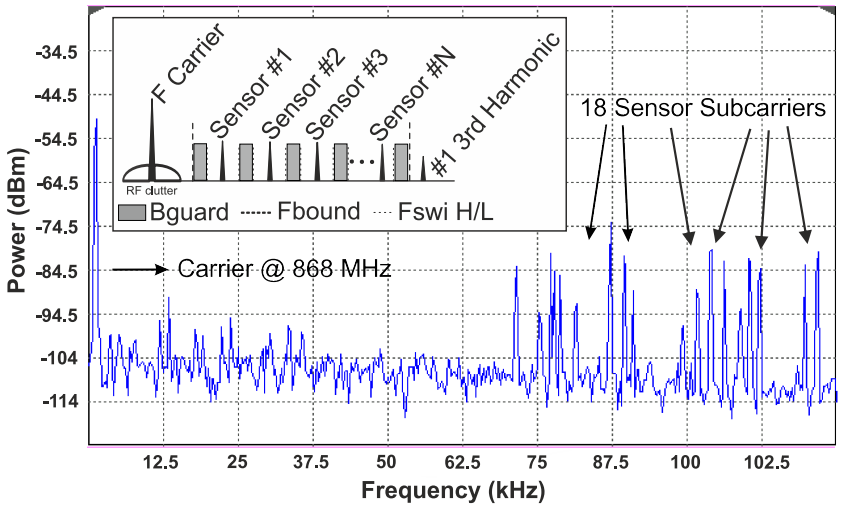

Figure 2.7: Inlay figure with concept and frequency-division multiple access of simultaneously operating multiple tags; each tag operates in a different frequency band, while guard bands avoid adjacent-channel interference. *Measured* sensor network spectrum for sensors $\#1 - 18$.

A Matlab script was written in order to be calculated R_2 and C_p component values of each sensor. For the WSN design was used only the "interdigitated" sensors. With "parallel-plates", the specific capacitance values $C_{\mathrm{p,i}}$ were excessive and could not be found in the commodity electronics market. One solution was to be placed a capacitor in series with the sensor but after the export of sensor capacitance versus the output frequency, was observed that the relationship wasn't linear, so the second sensor design wasn't used for the WSN.

It is noted that the outdoor environment temperature variations affect each sensor's circuit operation. For example, the CSS555 timer exhibits a temperature drift of 40 ppm/°C and thus, for a tag/sensor with nominal subcarrier frequency at 105 kHz, an extreme change of 30°C in temperature offers a frequency drift of $(40 * 30 * 105000)/10^6 = 126$ Hz. For bandwidth of 1.5 kHz per sensor, the aforementioned frequency shift amounts to $126/1500 = 8.4\%$ of each sensors bandwidth and an SM error in the same order. For bandwidth per sensor 10 times higher, that drift would amount to only 0.84% error, with however reduced number of sensors in the available spectrum band. Thus, there is clearly a flexible tradeoff between scalability (in number of simultaneously operating sensors) and measurement accuracy.

For example, assuming operating (subcarrier) sensors' frequencies in 100 kHz-299 kHz, guard band of 1 kHz (to avoid adjacent-channel interference between sensors) and 1.5 kHz bandwidth/sensor, the capacity of the network results to 79 sensors. The upper limit of 299 kHz is selected in order to avoid the odd order harmonic of the lower limit subcarrier frequency of 100 kHz. Future work will install low-cost envelope detector receivers in each sensor, so that a subset of the sensors operate simultaneously and thus, the same number M of subcarrier frequencies is shared by a larger number N of sensors, where $N >> M$ (resembling GSM network architecture, where the same frequency channel is used by 8 users in TDMA mode).

2.4 Power Consumption & Tradeoff

The power supply circuit of each sensor is a crucial part, since its lifetime depends on it. For this purpose, a voltage reference integrated circuit (IC) and a coin battery were utilized. The power source was a 300 mAh, 3 V lithium-ion battery (type CR2032), connected with the C2F converter through the voltage reference component (Texas Instruments (TI) REF3318, [39]). The voltage reference consumed 5 uA only and supplied with stable voltage (V_{cc}) the whole circuit.

The total power dissipation of each sensor is calculated below:

$$P_{\text{sensor}} = P_{\text{charge}} + P_{\text{quiescent}}, \tag{2.20}$$

with P_{charge}, the average power required for charging the capacitors and $P_{\text{quiescent}}$, the quiescent power dissipated by the timer and the voltage reference IC. The components that were utilized in the sensor design consumed quiescent power of $P_{\text{quiescent}} = 17.87\ \mu$W. Moreover, average charging power was calculated according to [32] as:

$$P_{\text{charge}} = \frac{V_{\text{cc}}^2}{6R_2 \ln(2)}. \tag{2.21}$$

It can be seen that average power during charging P_{charge} depends on the fundamental (subcarrier) frequency, through resistor R_2. Consumption and lifetime

Table 2.3: Power consumption example for two sensor nodes.

Sensor #	V_{cc} (V)	R_2 (kΩ)	F_{sw} (kHz)	P_{tot} (μW)	Life (months)
1	1.8	3.6	70	267.7	5.2
2	1.8	0.793	150	1152	0.44

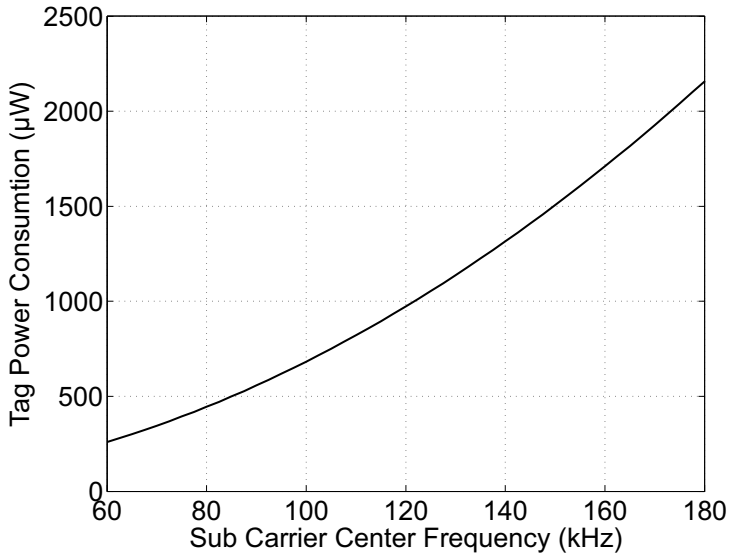

Figure 2.8: Total power consumption versus sensor subcarrier frequency.

example of two sensors is offered in Table 2.3, including the corresponding resistor values, center frequency value and V_{cc}. The lifetime is the duration of continuous (non-duty-cycled) operation with the utilization of the above battery. It is obvious that the lifetime of sensor #2 is too short due to the increased subcarrier center frequency. Fig. 2.8 presents the simulated power consumption of sensors as a function of subcarrier frequency. It is observed that when the center frequency of tags is increased from 60 kHz to 180 kHz, the power consumption is also (non-linearly) increased, with maximum value in the order of a mWatt; such relatively small power can be accommodated from various ambient solar, kinetic [40] or even thermoelectric [41] sources.

Scatter radio communication also depends on the RF clutter, i.e., the increased noise power spectral density around the carrier frequency. RF clutter is created due to reflections from the surrounding environment, as well as emitter's inherent

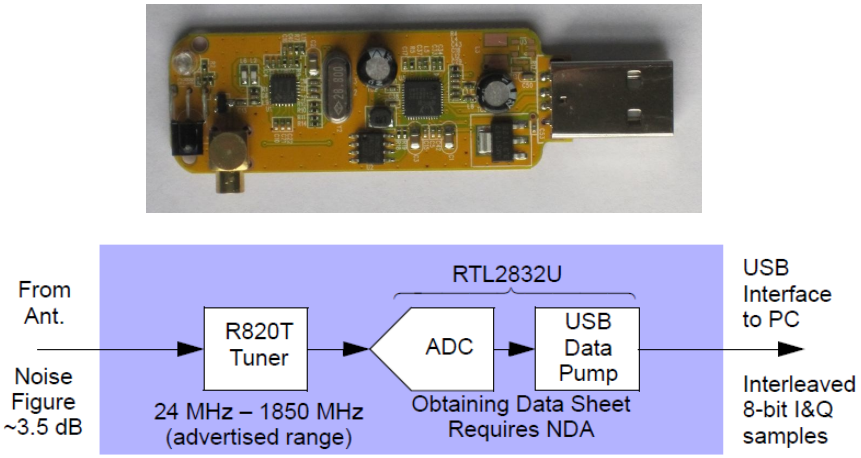

Figure 2.9: PCB picture (Up) and high level block diagram (Down) of the RTL-SDR.

phase jitter and non-linearities. Therefore, it is desirable for tags to operate as far as possible from the emitter's carrier frequency (i.e., as high as possible F_{sw}) in order to avoid increased noise power and hence, reduced signal-to-noise ratio. However, increased subcarrier frequency also increases power consumption and thus, reduces sensor's lifetime.

2.5 Ultra-Low Cost WSN Receiver

One of the most important components of the scatter radio WSN is the receiver of the backscattered signals. The receiver is responsible for the fundamental frequency estimation of the incoming scattered subcarrier signals. In this work, the ultra-low cost Realtek (RTL) software-defined radio (SDR) was employed, that uses a DVB-T TV tuner dongle based on the RTL2832U chip (Fig. 2.6, left and Fig. 2.9, up). It consists of an RF front-end and the Rafael Micro R820T tuner with frequency band range of 24-1766 MHz. A frequency synthesizer inside the R820T generates a local oscillator (LO) signal which is responsible for down converting the received RF to an intermediate frequency (IF). The tuning resolution is 1 Hz, or so it seems from the information available on the net. Gain control is also provided, both at the low noise amplifier (LNA) and at the output via a

variable gain amplifier (VGA). The term automatic gain control (AGC), refer to the use of a signal strength sensing circuit/algorithm to feedback a control signal to the gain control circuitry of an RF receiver. In this case that is the VGA and perhaps the LNA. The RTL2832U is the part, where the digital signal processing (DSP) takes place, which includes additional filtering and down sampling of the IF signal delivered by the R820T (Fig. 2.9, down).

The small cost on the order of a few Euro comes at the price of low dynamic range, since RTL offers only 8-bit resolution analog-to-digital converted (ADC) samples, pushed to a host computer through USB. A dipole 75 Ohm antenna was also designed to operate around 868 MHz. After a miniature coax connector for the antenna, there is a LNA with noise figure (NF) of about 3.5 dB. The measured, reported in specifications, signal-to-quantization noise ratio dynamic range is below 8bit $\times$ 6.02dB/bit + 1.76 [42], in the order of 43 dB, probably due to additional noise in the RTL front end, before the analog-to-digital converter (ADC).

The RTL SDR down-converts the signals to the baseband using a homodyne architecture and transfers the in-phase (I) and quadrature (Q) digitized signal samples to the host via USB port. Subsequently, the samples are saved to a queue (through GNU-Radio software) and processed in a software algorithm, implemented in MATLAB. In order to read each sensor node with RTL SDR, the fundamental subcarrier frequency $\hat{F}_{\mathrm{i}}$ of the i-th sensor was estimated using the periodogram technique, which in turn is grounded on maximum likelihood principles. The estimated subcarrier was given according to:

$$\hat{F}_{\mathrm{i}} = \underset{F\in[F^{\mathrm{L}}_{\mathrm{sw,i}},F^{\mathrm{H}}_{\mathrm{sw,i}}]}{\arg\max} |X(F)|^2, \tag{2.22}$$

where $X(F)$ is the Fourier transform of the baseband down-converted and carrier frequency offset (CFO)-compensated signal. CFO estimation and compensation was based on standard periodogram techniques [43]. $F^{\mathrm{L}}_{\mathrm{sw,i}}$ and $F^{\mathrm{H}}_{\mathrm{sw,i}}$ mark the a-priori known lowest and highest possible frequency output of the i-th tag. Thus, the frequency component with the maximum power at each spectrum band is estimated as the corresponding sensor's output frequency. The receiver Matlab code is attached in Appendix 5.1.

Table 2.4: Calibration function and fitting error.

Model	Fitted function	RMSE
3D	$f(x,y) = 105.5 + 0.232x + 0.0121y - 0.0074x^2$ $+0.0020xy - 0.0036y^2 + 7.531 * 10^{-5}x^3$ $-2.94 * 10^{-5}x^2y + 2.08 * 10^{-6}xy^2 + 3.65 * 10^{-5}y^3$	0.23 (kHz)

2.6 Calibration

Deviations from nominal values of each tag's components (e.g., tolerance of capacitors, resistor or timer), as well as temperature dependence, require compensation, i.e., sensor calibration; the tags of this work were calibrated using polynomial surface fitting, utilizing both %SM and temperature parameter as input variables, as described below.

A soil sample was taken from the field, dried and filled a 1000 cubic centimetre (cc) container. Specific mass of water (in grams) was poured into the container and soil moisture percentage by volume was calculated, according to the following:

$$\text{Soil Moisture (\%) by Volume} = \frac{\text{Volume of Water}}{\text{Volume of Soil}} \times 100, \tag{2.23}$$

with

$$\text{Volume of Water} = \frac{\text{Mass of Water}}{\text{Density of Water}}, \tag{2.24}$$

with (well-known) density of water equal to 1 gram per cc.

Using the sensor design and the WSN reader described above, samples of subcarrier frequency were collected, for fixed temperature and variable soil moisture % (or vice versa). Working with 226 sets of measurements (subcarrier frequency, temperature and soil moisture), minimum mean square error (MSE) cubic polynomial fitting was applied between subcarrier frequency, %SM and temperature. The outcome polynomial is given in Table 2.4 with corresponding fitting root mean squared error (RMSE). The surface (3D) transfer function is shown in Fig. 2.10 and a special case for fixed temperature 18.4°C, (2D) transfer function is shown in Fig. 2.11.

Fig. 2.11 shows an interesting saturation effect (at the output frequency), when

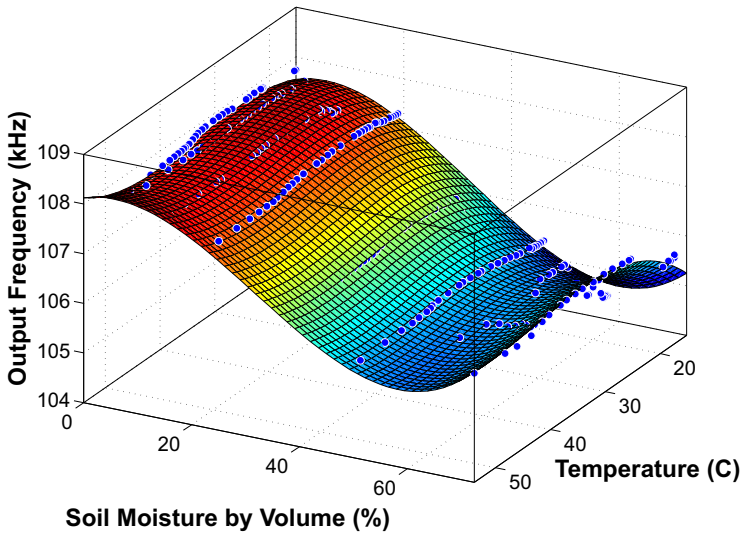

Figure 2.10: Measured soil moisture (%) characteristic and polynomially-fitted function versus frequency and temperature for sensor #8. The data measurements were 226 sets of soil moisture, temperature and output frequency samples.

the soil moisture by volume reaches 48%. That is due to the hydraulic properties of all soil textures. Specifically, *"total pore space, expressed on a volumetric basis, ranges from* 40% *in sandy soil to* 48% *in clay soil. When a soil is completely saturated, all the pores are filled with water. Thus, porosity is also the water content at saturation, expressed as the volume of water per volume of soil."* [44, chapter 6 "Soils", p. 167]. Thus, the observed saturation above 48% of the sensor is clearly coherent with the physical phenomenon of water content in various soil textures and thus, an indirect indication that the sensor is working properly.

Measured %SM results using the above procedure of (2.23), (2.24) were compared with the sensor's output; for data of Fig. 2.11 (fixed temperature), root mean squared error (RMSE) of 0.15% SM and mean absolute error (MAE) of 0.13% SM were found. Such error will be denoted as *calibration error*, since it does not include the error due to scatter radio communication, studied below.

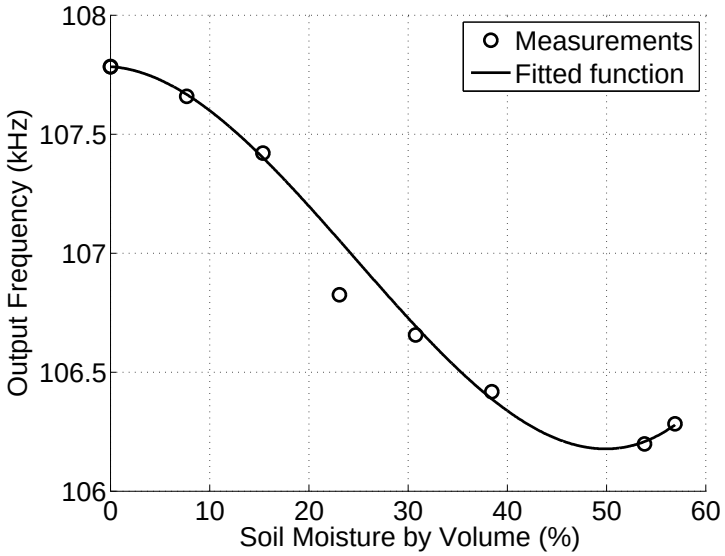

Figure 2.11: Measured soil moisture (%) characteristic and fitted function versus frequency for sensor #8 for fixed environmental temperature (18.4°C).

2.7 Experimental Results

Fig. 2.6 (right picture) depicts one of the fabricated sensor tags with low-cost FR-4 material and cost on the order of 6 Euro. At the installation site, each backscatter sensor node's bow-tie antenna (with its scatter radio front-end) was located well above the ground, while the fabricated capacitive sensor was inserted into the soil (Fig. 2.13) and the connection between those two parts was established with cables. The implemented demonstration WSN consisted of 18 scatter radio soil moisture sensors nodes, which could operate simultaneously, without collisions; Fig. 2.7 depicts the obtained sensors subcarriers and the emitter carrier at 868 MHz. The PCBs of 18 tags are depicted in Fig. 2.12. Tag board schematic and layout is showed in (Appendix) Fig. 5.1 and in Fig. 5.2, respectively.

Each sensor was allocated a unique 0.5 to 1.5 kHz frequency band (bandwidth) and there was a guard-band of 1 kHz between neighbouring-in-frequency tags to alleviate adjacent channel interference. Fig. 2.7 illustrates the subcarriers corresponding to 0% SM. For demonstration purposes, a subset of the network was deployed in the indoor garden of Technical University of Crete. The bistatic topology scatter radio WSN with eight sensor nodes is depicted in Fig. 2.13. Carrier

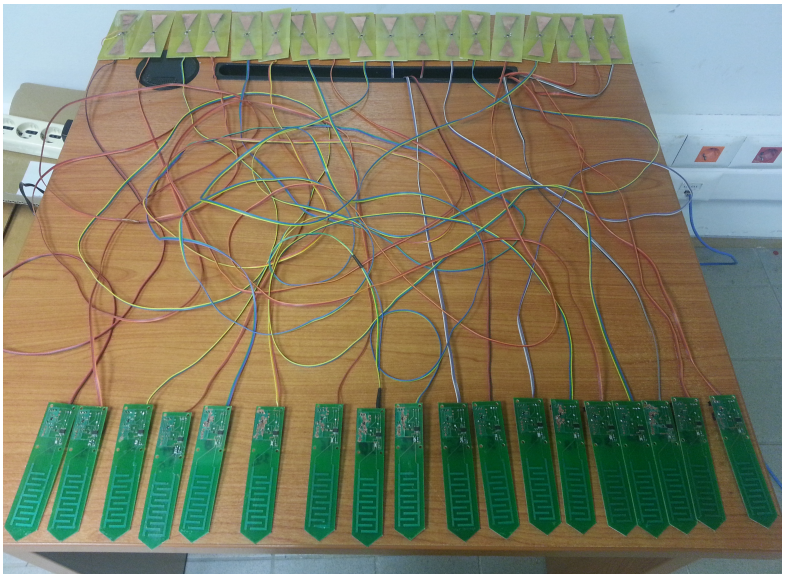

Figure 2.12: 18 Soil Moiture Sensor Tag Designs.

emitter (E) and RTL-SDR reader (R) were located at either sides of the field with the sensors in between. Capacitive sensors were inserted into the soil near the root of each plant, while the scatter radio front-ends were placed 1.5 meter above the ground, using canes.

Sampled data time series collected from approximately seven hours of continuous monitoring are illustrated in Fig. 2.14. It can be easily observed that after the watering instances, the output frequency of the sensors changed instantly, while it settled after a limited amount of time.

In order to achieve both communication performance characterization and sensing accuracy of the proposed WSN, maximum communication range and end-to-end sensing accuracy were experimentally measured. Specifically, a complete bistatic topology link was utilized outdoors (Fig. 2.15).

Carrier emitter, SDR receiver and sensor/tag (with subcarrier center frequency at 109 kHz) were installed at 1.3 m height. Temperature of 18°C was measured, soil moisture was fixed at 0% SM (corresponding to 109 kHz subcarrier frequency for the specific sensor), sampling rate was set to 1 MHz and duration of 100 ms was exploited per sensor measurement. Communication performance was tested for various installation topologies and the corresponding results, in terms of estimating

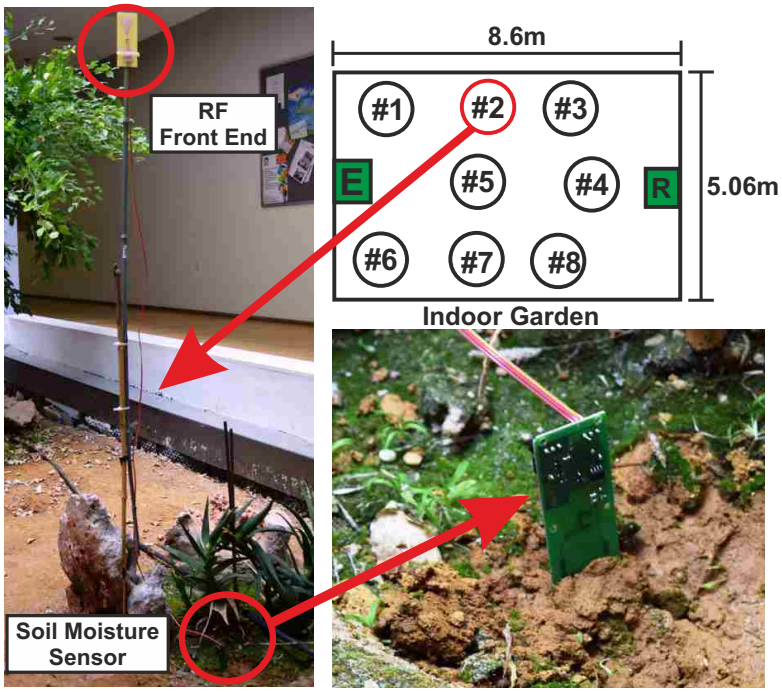

Figure 2.13: Bistatic soil moisture sensor network demonstration; capacitive soil moisture sensor in installed into the ground, while scatter radio antenna is well above ground and being illuminated by the carrier emitter (E), while backscattered signal from various tags is received by the reader (R).

the transmitted subcarrier frequency, are presented in Table 2.5, as a function of emitter-to-tag distance (d_{et}), tag-to-reader distance (d_{tr}) and root mean squared error (RMSE) in Hz, after 1000 measurements, for each case (row) of Table 2.5. Reference subcarrier value was measured with carrier emitter and SDR receiver in closed proximity with the sensor (and all the rest of the parameters the same), using average value out of 1000 sensor measurements.

Sensor-receiver ranges in the order of 256 meter are possible, with limited RMSE error in the order of 0.1%, due to wireless communication. Such small *communication error* suggests that communication ranges could be further increased and scatter radio communication range is not an issue. A similar finding, based on proper designs for scatter radio reception, has been also recently reported in [45–47]. Therefore, the overall sensor error is upper bounded by the sum of the RMSE calibration and communication errors under mild assumptions (e.g., independence of noise in sensor and and noise in receiver, unbiased errors etc.),

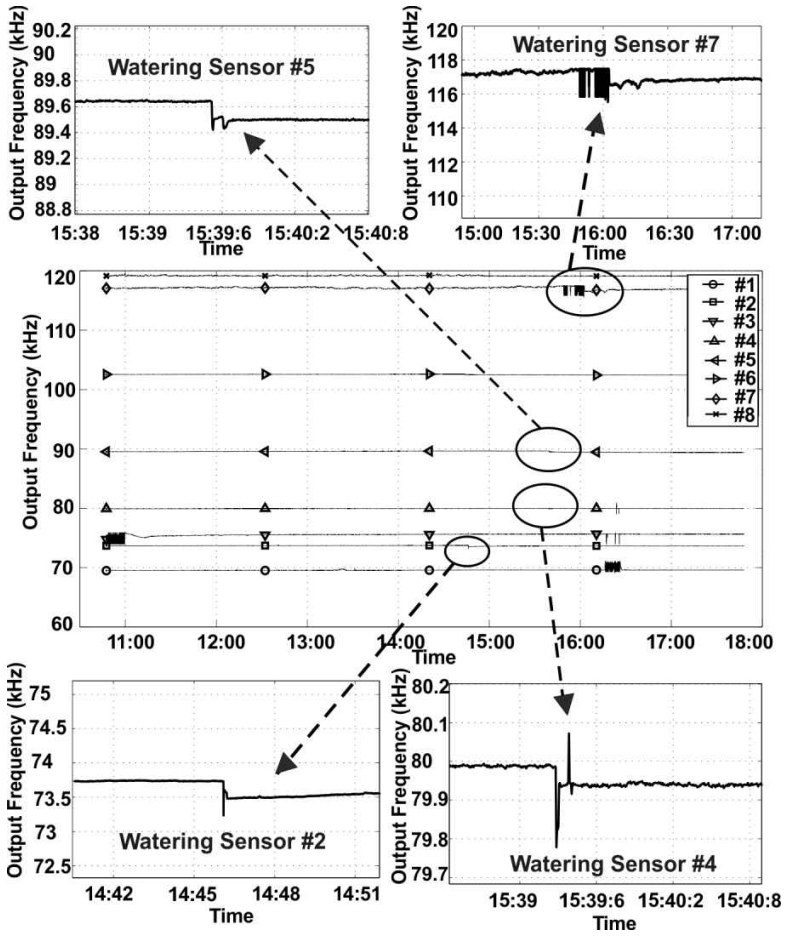

Figure 2.14: Simultaneous and continuous soil moisture sensing from 8 tags, as a function of time, using the proposed scatter radio sensor network.

which for the above values of Table 2.5 and the results of Section 2.6 offers overall RMSE below 1% SM. Finally, it is noted that for all experimental results, emitter transmission power was 13 dBm at 868 MHz.

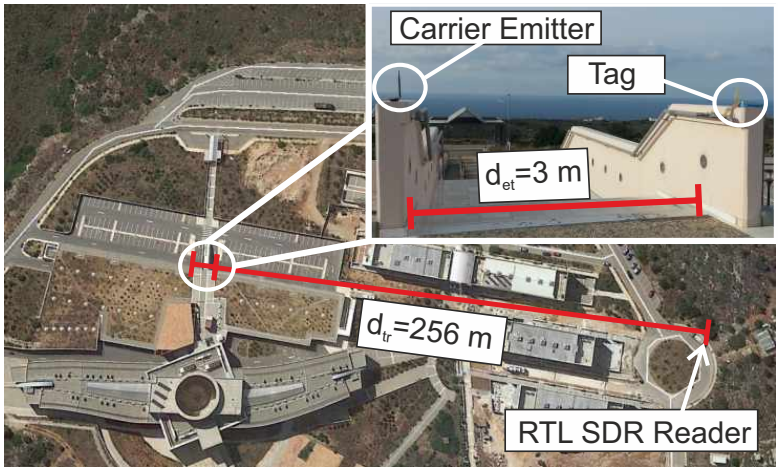

Figure 2.15: Testing outdoors the communication range of the specific bistatic analog backscatter architecture.

Table 2.5: Communication Accuracy.

#	d_{et} (m)	d_{tr} (m)	RMSE (Hz)	RMSE (%)
1	3	48.3	12.91	0.011
2	3	69	17.00	0.015
3	3	146	26.89	0.024
4	3	205	31.39	0.028
5	3	256	35.28	0.032
6	8.4	60.8	21.41	0.019
7	8.4	138	32.63	0.029
8	21.4	126	9.70	0.008

Chapter 3

Dual Band RF Harvesting & Low-Power Supply System

Nowadays an ocean of electromagnetic waves surrounds us, most of that ambient electromagnetic energy remains unused. Globally, the number of radio frequency (RF) emitters has been continuously increasing, due to widespread use of wireless technologies, such as cellular networks, Wi-Fi, digital TV and wireless sensor networks (WSN). Collection of ambient RF energy and its use of powering electrical devices is an engineering challenge [48]. Over the last years, wireless power transfer (WPT) based on far-field electromagnetic radiation is recommended for large amount of sensors due to their necessity to be autonomous and self-sustained in power [11], while battery replacement is a lengthy and costly procedure in large sensor networks. This WPT concept is suitable for Internet of Things (IoT) applications such as environmental WSNs and sensor networks for smart cities. The collection of unused ambient RF energy with rectifiers and supply of backscatter radio WSNs (sensors of first part of this work) [21], [32] for example, is a great engineering challenge. In this work, FM and VHF-UHF carrier emitters (e.g., in bistatic scatter radio sensor networks [45], [46]) will be considered as potential RF power sources. On the other hand, ambient RF energy harvesting offers a rela-

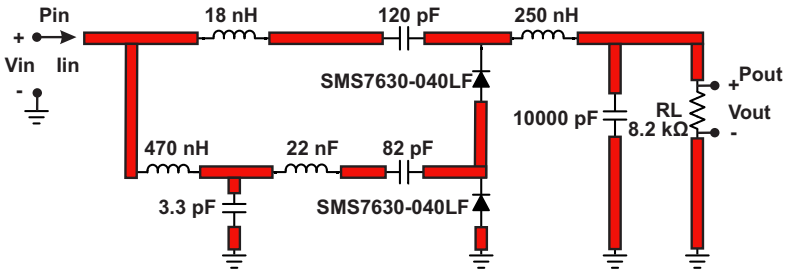

Figure 3.1: The double diode rectifier design.

tively low energy density of some uW/cm^2, compared to other power sources (e.g.

solar energy or energy from soil [49]), however it can operate in hybrid mode, in conjunction with multiple other sources [16]. Efficiency is an important parameter in a rectifier topology, i.e. the ratio of DC output power to RF input power. Nowadays, significant research effort has been directed towards high-efficiency rectifiers. Many attempts emphasize on the required impedance matching circuit inductances, while minimizing reflection coefficient. For example, RF-to-DC rectification efficiency of 20.5% and 35.3% was attained in [15] for -20 dBm and -10 dBm input power, respectively.

3.1 Rectifier

3.1.1 Rectifier Design and Analysis

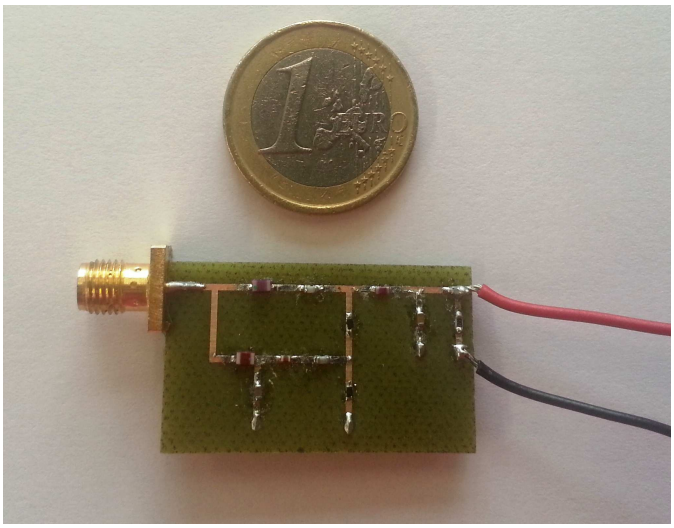

Figure 3.2: The fabricated top layer of the rectifier.

In this work, an efficient low-cost and low-complexity rectifier is developed for low-power input. The rectifier is based on double rectification circuit with single diodes as depicted in Fig. 3.1. The RF input power is converted to DC power through the low-cost Schottky diodes (SMS7630-040LF). The matching circuit (inductors combined with capacitors) reduces the reflection losses of the incoming wave, while the rectifier was designed to operate at 868 MHz (UHF ISM frequency

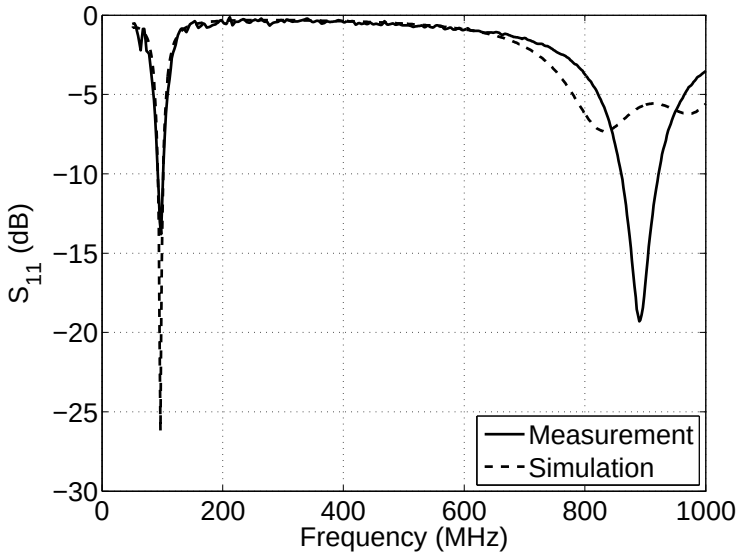

Figure 3.3: Reflection coefficient at the input of rectifier.

in Europe) and at 97.5 MHz (center of FM band), simultaneously. Harmonic-balance and Momentum solver was employed for simulations. The FR-4 substrate was modelled with $\epsilon_{\mathrm{r}} = 4.4$, $\tan\delta = 0.025$, copper thickness 35 μm and substrate height 1.6 mm. The first goal of modelling and simulation was the maximization of the RF to DC efficiency:

$$\eta = \frac{P_{\mathrm{out}}}{P_{\mathrm{in}}} = \frac{V_{\mathrm{out}}^2/R_L}{P_{\mathrm{in}}}, \tag{3.1}$$

with P_{in}, P_{out} the input and output power and V_{out} the voltage across the load R_L. The second goal was the minimization of reflection coefficient,

$$\Gamma_{in} = \frac{Z_{in} - 50}{Z_{in} + 50}, \tag{3.2}$$

for input power P_{in} −20 dBm at 868 MHz and 97.5 MHz. The input impedance Z_{in} is defined as (Fig. 3.1):

$$Z_{in} = \frac{V_{in}}{I_{in}}. \tag{3.3}$$

After optimization, the dual-band prototype was implemented with discrete components and fixed trace dimensions, as shown in Fig. 3.2. The load at the

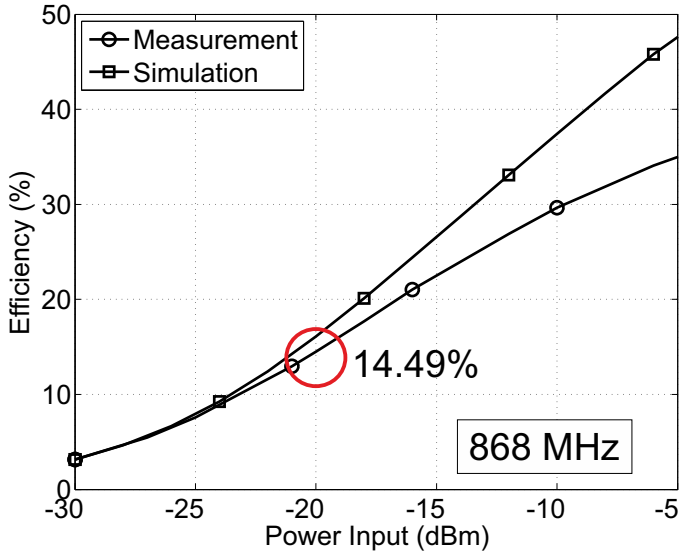

Figure 3.4: Rectifier efficiency versus total power input at 868 MHz.

output (R_L) was fixed at 9.2 kOhm. Measurements were employed after that, using a signal generator and a voltmeter. The simulated and measured reflection coefficient S_{11} is depicted in Fig. 3.3. Reasonable agreement between predicted and measured results is observed at both frequency bands. Figs. 3.4 and 3.5 depict efficiency η versus P_{in} for measurement and simulated results for the two separate bands. According to measured results, the efficiency is 14.49% and 27.44% at 868 MHz and 97.5 MHz, respectively for $P_{\text{in}} = -20$ dBm. For $P_{\text{in}} = -10$ dBm the results are 29.64% and 46.58.% for 868 MHz and 97.5 MHz, respectively.

The simulated efficiency versus frequency for three power input levels is depicted in Fig. 3.6. As expected, the rectifier operates optimally at 868 MHz and 97.5 MHz. Figs. 3.7 and 3.8 show the relationship between rectifier efficiency and load. Frequency is now fixed at 868 MHz for Fig. 3.7 and at 97.5 MHz for Fig. 3.8. It is observed that the 9.2 kOhm load is appropriate for 868 MHz but not for 97.5 MHz. Finally, Fig. 3.9 offers the measured open circuit voltage (without load) versus input power, for the two frequency bands. As expected, the relationship is not linear due to the non linearity of the discrete components.

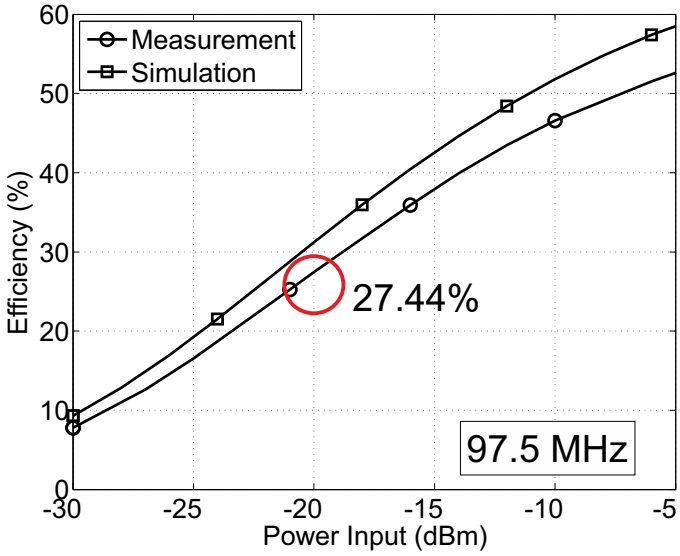

Figure 3.5: Rectifier efficiency versus total power input at 97.5 MHz.

3.2 Antenna Design

In order to supply the rectifier with wirelessly harvested power, a microstrip multi-band antenna was designed and fabricated. Specifically, a hybrid microstrip monopole antenna was designed to operate at ISM band (around 868 MHz) and at FM band (around 100 MHz). The design is a variation of a monopole antenna (of wide-band operation) with a loop for FM band resonance (and low fabrication complexity) on FR-4 substrate. The fabricated antenna is depicted in Fig. 3.10 and its measured reflection coefficient is depicted in Fig. 3.11.

3.3 Boost Converter

In this work, the low-power boost converter Texas Instrument "bq25504" was utilized [50]. The latter is an integrated-circuit with maximum power point tracking (MPPT), minimum cold start voltage and typical input power of 330 mV and 10 μW, respectively, and low quiescent current ($\leq$ 330 nA). Hence, for minimum voltage of 330 mV and typical power of 10 μW, the boost converter input impedance is 10890 Ohm, which is close to 9200 Ohm (i.e. the load value for optimum RF

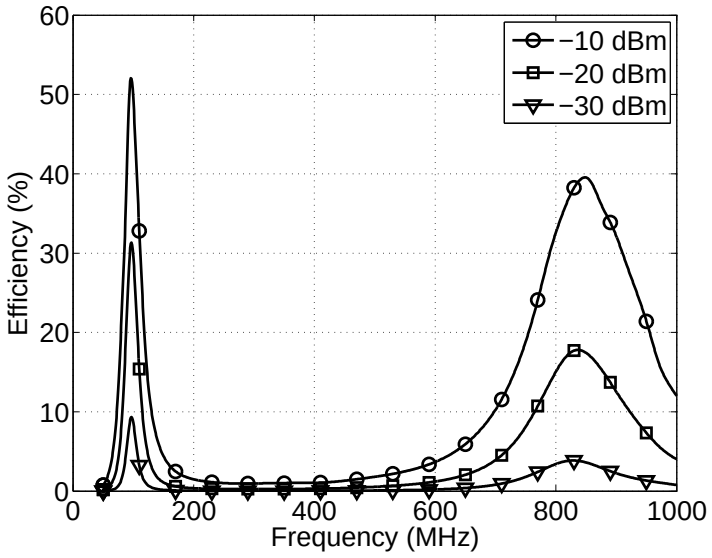

Figure 3.6: Rectifier efficiency versus frequency for different power inputs.

to DC efficiency of the proposed rectifier). However, due to the MPPT function (which aims to extract the maximum power from the rectifier output), as well as the fact that the boost converter has two main operational modes (one for cold-start operation and one after cold-start, with main boost charger enabled), the input impedance does not remain constant. The MPPT functionality includes periodic sampling of the input (open) voltage signal, after disabling the charger for a limited duration of time (on the order of 256 ms every 16 sec); the cold start charger is an unregulated, hysteretic boost converter with lower efficiency compared to the main boost charger and provides the initial power so that the latter can start its operation. This work measured experimentally the end-to-end input-output relationship of the whole system, as described below.

The rectifier was designed to connected to the analog backscatter sensor node through the "bq25504". Fig. 3.12 depicts the circuit schematic topology. Rectifier voltage ($V_{\rm oc} \equiv V_{\rm IN\_DC}$) was boosted ($V_{\rm BAT}$) and a 100 μF capacitor was charged from 0 V. It is noted that the boost converter was self-started (cold start) and no external energy was used. Digital signal output ($V_{\rm BAT\_OK}$) is set to high and low, when the capacitor voltage reaches a pre-defined upper and lower limit, respectively. In this work, the boost converter was designed to have low and upper

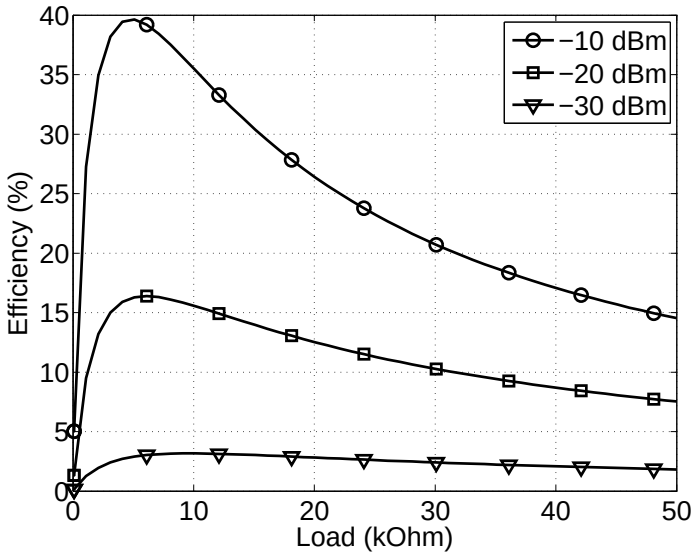

Figure 3.7: Rectifier efficiency for 868 MHz versus load for different power inputs.

voltage threshold 2.4 V and 2.8 V, respectively.

An external PMOS ("BSH207") was placed between the output load (in our case is a LED, for future work will be a scatter radio sensor node) and the V_{BAT} pin. The inverted $V_{\mathrm{BAT\_OK}}$ signal (through the open drain NMOS "BSH105") was used to drive the gate of the PMOS. While V_{BAT} is lower than 2.8 V, PMOS stays off (zero current) and the boost converter charges the capacitor. Next, when the V_{BAT} reaches 2.8 V, PMOS turns on and energy flows from the capacitor to the LED. Next, capacitor is discharged and when $V_{\mathrm{BAT}} = 2.4$ V, PMOS turns off again and current stops flowing to the LED. Then, the capacitor is charged again until $V_{\mathrm{BAT}} = 2.8$ V and the procedure is repeated. A data acquisition (DAQ NI USB-6356) instrument was used in order to measure the voltage across the rectifier output ($V_{\mathrm{IN\_DC}}$) and the capacitor (V_{BAT}). The measurement setup is depicted in Fig. 3.13 and charge-discharge operation of the LED can be observed in Fig. 3.14 for 800 seconds duration. The rectifier P_{in} was -15 dBm at 97.5 MHz. Finally, it is noted again that the boost converter was self-started and no external energy was used. The boost converter with the MOSFET switches was designed and constructed in one PCB as is depicted in Fig. 5.3 (board schematic), Fig. 5.4 (board layout) and Fig. 5.5 (PCB).

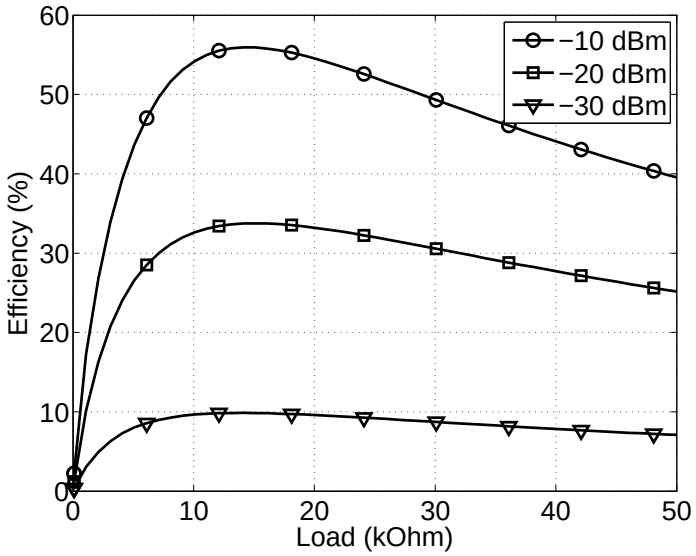

Figure 3.8: Rectifier efficiency for 97.5 MHz versus load for different power inputs.

3.3.1 End-to-End Efficiency

The duty cycle of the LED can be used to calculate the efficiency of the system and according to [51], the total end-to-end efficiency of the whole system is:

$$\eta_{total} = \frac{E_{DC}}{E_{in}} = \frac{C_s \frac{V_{BAT,high}^2 - V_{BAT,low}^2}{2}}{\int_0^{t_{cycle}} P_{in}\,\mathrm{d}t}. \tag{3.4}$$

E_{DC} is the boost converter output, DC energy and E_{in} the rectifier input energy. E_{in} can be calculated by integrating the time averaged P_{in} over a cycle time t_{cycle}.

The cycle time is the charge-discharge time of the storage capacitor between $V_{BAT,high}$ and $V_{BAT,low}$. From measurements of Fig. 3.14, E_{DC} was calculated at 265.17 uJ with C_s=100 uF and t_{cycle} was measured at 38.9 sec. The obtained end-to-end efficiency for $P_{in} = -15$ dBm and is 21%.

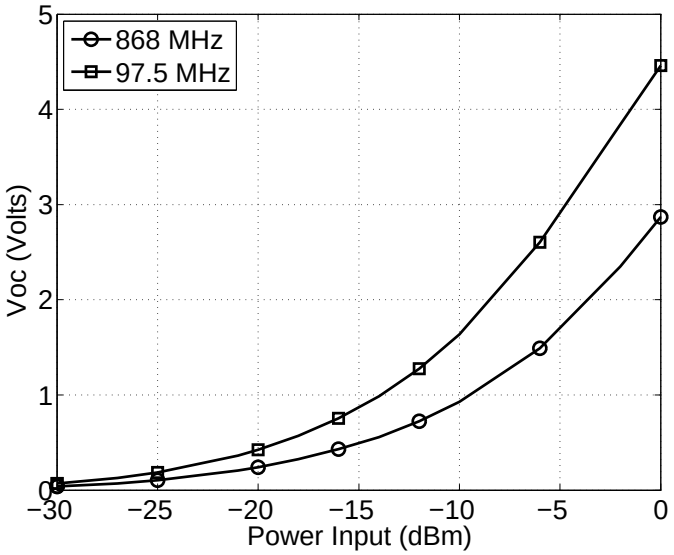

Figure 3.9: Measured rectifier output open circuit voltage for 97.5 MHz and 868 MHz.

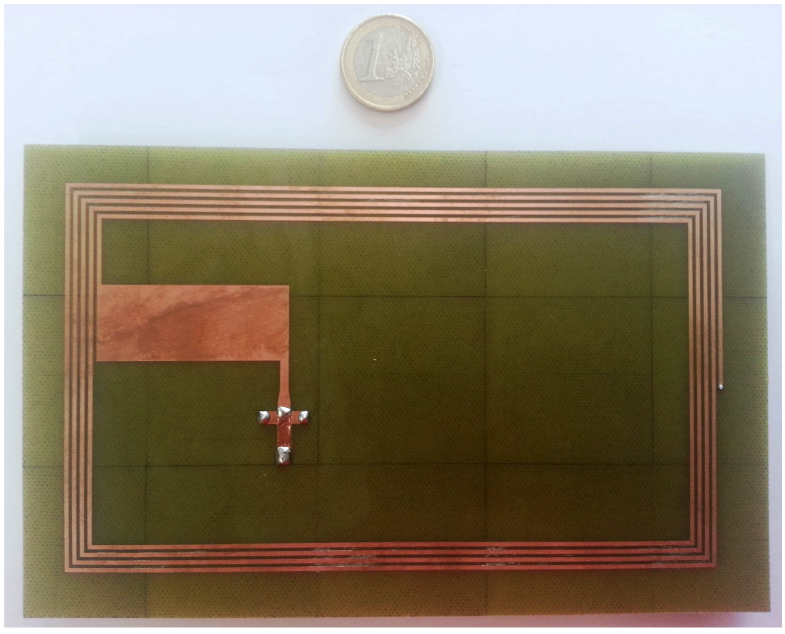

Figure 3.10: The fabricated multi-band antenna.

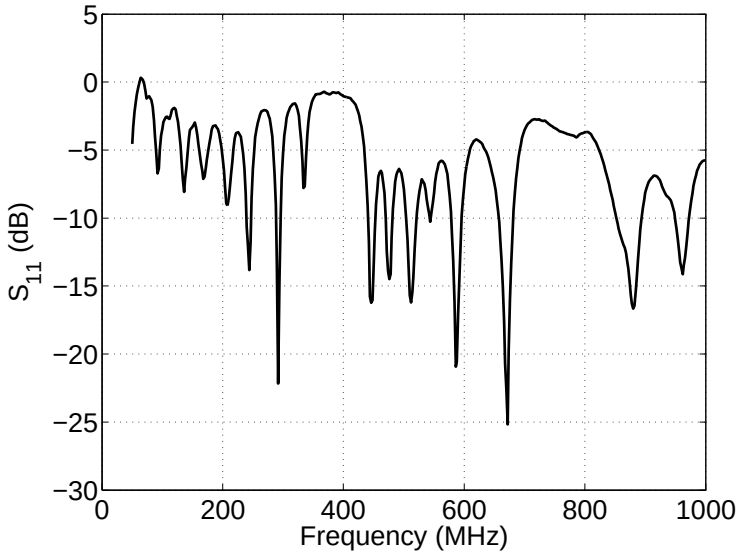

Figure 3.11: Reflection coefficient of the multi-band antenna.

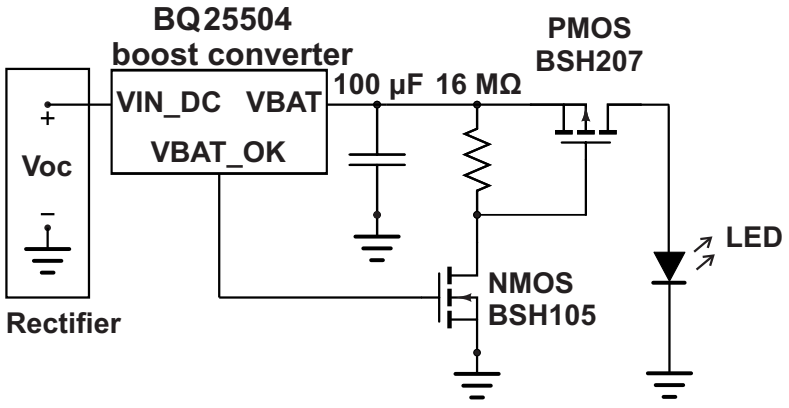

Figure 3.12: Boost converter schematic with the low-power BQ25504.

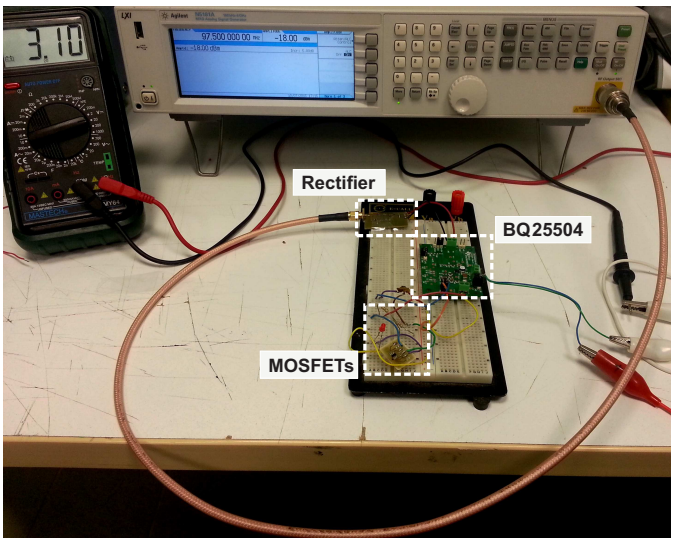

Figure 3.13: Measurement setup with rectifier, signal generator, boost converter and MOSFET transistors.

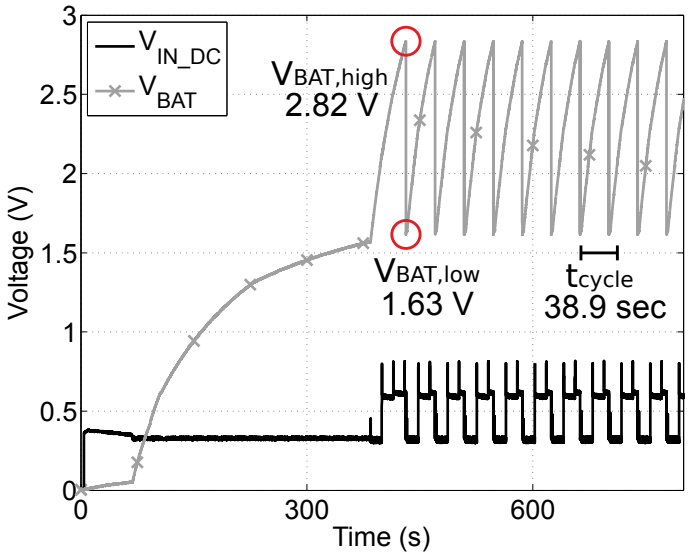

Figure 3.14: Boost converter input (V_{IN_DC}) and output (V_{BAT}) voltage measurement for $P_{in} = -15$ dBm and F = 97.5 MHz. Voltage V_{BAT} is the voltage across 100 uF capacitor, and V_{IN_DC} is the open circuit voltage of rectifier output.

Chapter 4

Conclusions

4.1 Conclusion

The first part of the thesis describes in detail the development of an ultra-low power and cost scatter radio network for soil moisture. Communication ranges in the order of 250 meter were experimentally demonstrated, with overall RMSE, less than 1%. Scaling issues were also discussed. The power consumption of each scatter radio sensor is in the order of 200 μW.

The second part presents the design and implementation of a dual band RF rectifier system with a commodity DC-DC converter. Its high efficiency and tested operation at low-power input could perhaps enable the proposed WSN powered by ambient RF. The circuit was designed with two single diodes, on a low-cost, lossy FR-4 substrate. The system collects the RF energy from scatter radio emitters at 868 MHz and from one FM frequency at 97.5 MHz. Also a multi-band antenna was designed and constructed. Experimental results with a commodity DC-DC converter from cold-start were also presented and discussed.

4.2 Future Work

Future work should be focused towards the development of a full FM band rectifier. The energy harvesting system will exploit all FM band frequencies and scatter radio emitters frequency in order to capture much more unused energy. Future efforts should aim to combine the capabilities of the two developed systems in order to design a battery-less scatter radio sensor having the FM band and emitters as a power source. Finally, an ultra large scale network of such sensor nodes should be exploited, with ultra low cost sensor nodes having capacitors as energy tanks.

Chapter 5

Appendix

5.1 Matlab Receiver Code

```
%Eleutherios Kabianakis
%Spyridon-Nektarios Daskalakis
close all;
clear all;
clc;

Fs = 250e3; % same as gnuradio
Ts = 1/Fs;

Resolution = 1; % in Hz
N_F = Fs/Resolution;
F_axis = -Fs/2:Fs/N_F:Fs/2-Fs/N_F;

%Subcarrier center Freq in Hz
SUB_CENTER = [109000];
%Sensors bandwidth
SUB_BW = 1.5e3;

%read samples from a fifo
fi = fopen('RTL_SDR_fifo', 'rb');

t_sampling = 1 ;        % seconds
N_samples = round(Fs*t_sampling);
t = 0:Ts:t_sampling-Ts;

```

```
26 counter = 0;
27 packets = 0;
28 plot1=1;
29
30 HIST_SIZE = 1000; %stop after 1000 irerations
31 F_sense_hist = zeros(HIST_SIZE,1);
32 hists = 0;
33
34 while(1)
35     x = fread(fi, 2*N_samples, 'float32'); % get samples
          (*2 for I-Q)
36     x = x(1:2:end) + j*x(2:2:end);          %
          deinterleaving
37     counter = counter + 1;
38
39     if mod(counter, 2) == 0
40         packets = packets + 1;
41         % fft
42         x_fft = fftshift(fft(x, N_F));
43         % cfo estimate
44         [mval mpos] = max(abs(x_fft));
45         DF_est = F_axis(mpos);
46         % cfo correction
47         x_corr = x.*exp(-j*2*pi*DF_est*t).';
48         % corrected cfo
49         x_corr_fft = fftshift(fft(x_corr, N_F));
50
51         % sensor's fft
52         LEFT = SUB_CENTER - SUB_BW;
53         RIGHT = SUB_CENTER + SUB_BW;
54         x_sensor_fft = x_corr_fft;
55         x_sensor_fft(F_axis < -RIGHT) = 0;
56         x_sensor_fft(F_axis > RIGHT) = 0;
```

```
57          x_sensor_fft(abs(F_axis) < LEFT) = 0;
58
59          %find subcarrier
60          [mval mpos] = max(abs(x_sensor_fft));
61          F_sensor_est = abs(F_axis(mpos));
62          mval2=10*log10((abs(mval).^2)*Ts);
63          F_sensor_power = mval2;
64          fprintf('N=%d|F=%5.1f|Power=%7.1f\n',packets,
                F_sensor_est,F_sensor_power)
65          F_sense_hist(packets) = F_sensor_est;
66
67          if plot1==1;
68              % plot
69              figure(1);
70              subplot(2, 1, 1);
71              plot(t, real(x_corr));
72              hold on;
73              plot(t, imag(x_corr), 'g--');
74              hold off;
75              drawnow;
76              subplot(2, 1, 2);
77                  semilogy(F_axis, (abs(x_corr_fft).^2));
78              grid on;
79              axis tight;
80              drawnow;
81          end
82                              if(mod(packets,HIST_SIZE) == 0)
83                                      return;
84                              end
85      end
86  end
```

5.2 PCBs

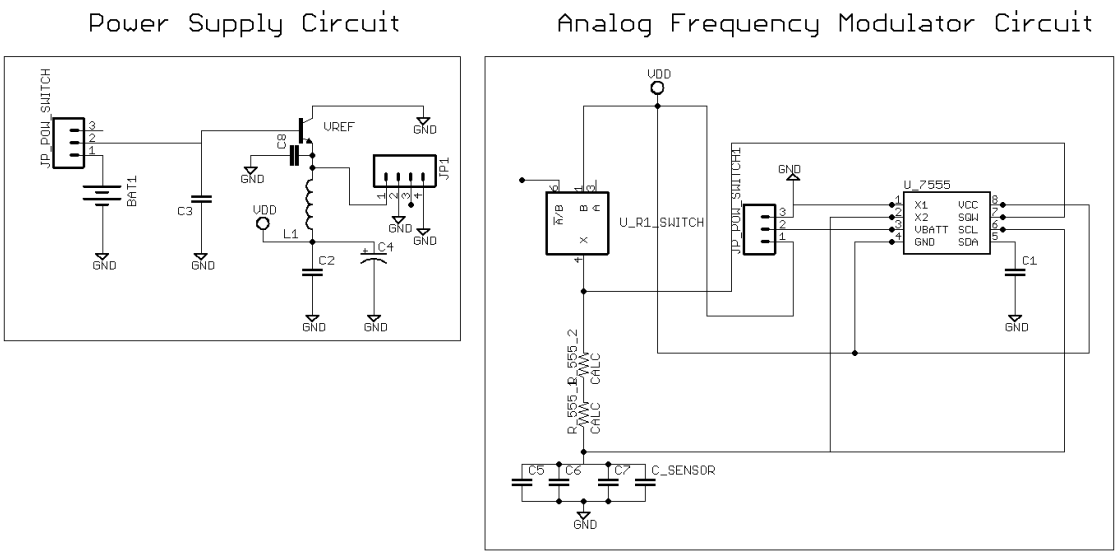

Figure 5.1: Schematic of the tag.

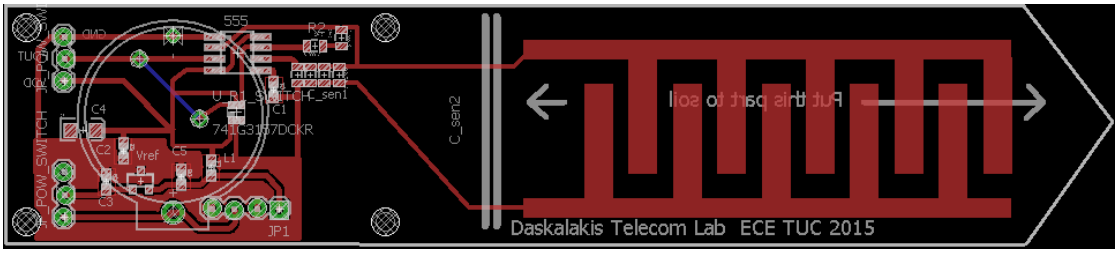

Figure 5.2: Tag PCB layout.

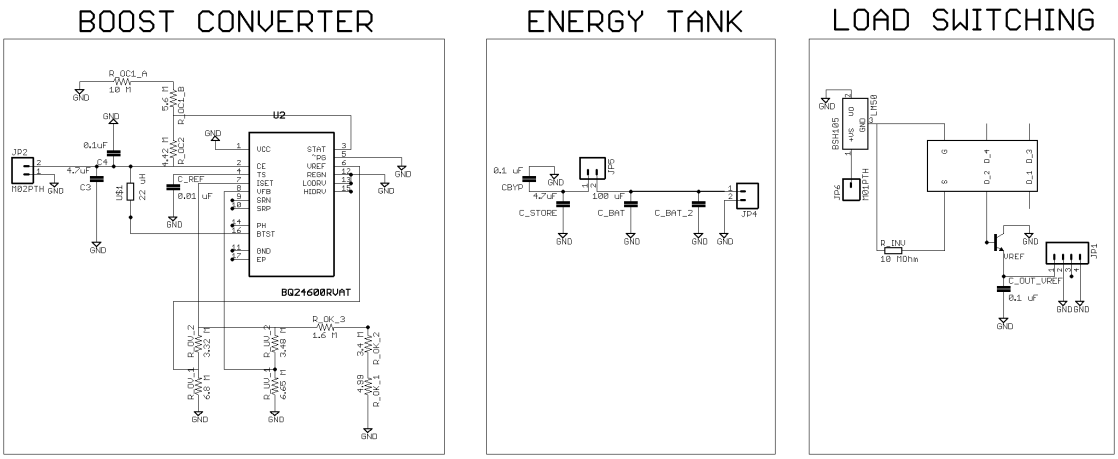

Figure 5.3: Schematic of the Ultra Low Power Boost Converter with Capasitor Management.

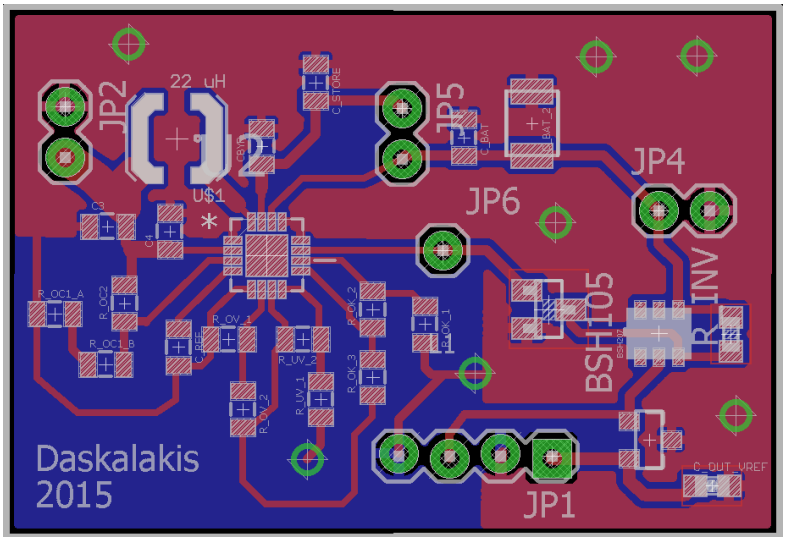

Figure 5.4: PCB layout of Ultra Low Power Boost Converter.

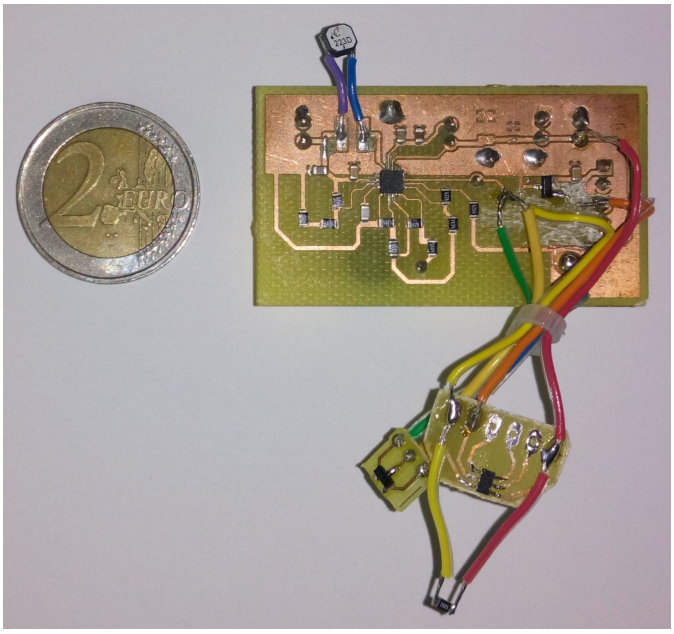

Figure 5.5: PCB of Ultra Low Power Boost Converter.

Bibliography

[1] G. Vellidis, V. Garrick, S. Pocknee, C. Perry, C. Kvien, and M. Tucker, "How wireless will change agriculture," *Precision agriculture*, vol. 7, pp. 57–68, 2007.

[2] M. Haefke, S. Mukhopadhyay, and H. Ewald, "A Zigbee based smart sensing platform for monitoring environmental parameters," in *Proc. IEEE Int. Conf. on Instrum. and Meas. Techn. (I2MTC)*, Binjiang, China, May. 2011, pp. 1–8.

[3] G. R. Mendez, M. A. M. Yunus, and S. C. Mukhopadhyay, "A WiFi based smart wireless sensor network for monitoring an agricultural environment," in *Proc. IEEE Int. Conf. on Instrum. and Meas. Techn. (I2MTC)*, Graz, Austria, May. 2012, pp. 2640–2645.

[4] D. Antolín, A. Bayo, N. Medrano, B. Calvo, and S. Celma, "Wubinet: A flexible WSN for applications in environmental monitoring," in *Proc. IEEE Int. Conf. on Instrum. and Meas. Techn. (I2MTC)*, Graz, Austria, May. 2012, pp. 2608–2611.

[5] V. Palazzari, P. Mezzanotte, F. Alimenti, F. Fratini, G. Orecchini, M. Virili, C. Mariotti, and L. Roselli, "Leaf compatible "eco-friendly" temperature sensor clip for high density monitoring wireless networks," in *Proc. IEEE 15th Medit. Microw. Symp. (MMS)*, Lecce, Italy, Dec. 2015, pp. 1–4.

[6] Y. Kawahara, H. Lee, and M. M. Tentzeris, "Sensprout: inkjet-printed soil moisture and leaf wetness sensor," in *Proc. ACM Conf. on Ubiquitous Computing*, Pittsburgh PA, USA, Sep. 2012, pp. 545–545.

[7] S. Sulaiman, A. Manut, and A. Nur Firdaus, "Design, fabrication and testing of fringing electric field soil moisture sensor for wireless precision agriculture applications," in *Proc. IEEE Int. Conf. on Inf. and Multim. Techn. (ICIMT)*, Jeju Island, South Korea, Sep. 2009, pp. 513–516.

[8] S. Kim, Y. Kawahara, A. Georgiadis, A. Collado, and M. Tentzeris, "Low-cost inkjet-printed fully passive RFID tags using metamaterial-inspired antennas for capacitive sensing applications," in *Proc. IEEE Int. Microw. Symp. (IMS)*, Seattle WA, USA, Jun. 2013, pp. 1–4.

[9] Y. Liu, Y. He, M. Li, J. Wang, K. Liu, L. Mo, W. Dong, Z. Yang, M. Xi, J. Zhao, and X.-Y. Li, "Does wireless sensor network scale? A measurement study on GreenOrbs," in *Proc. IEEE INFOCOM*, Shanghai, China, Apr. 2011, pp. 873–881.

[10] G. Vannucci, A. Bletsas, and D. Leigh, "A software-defined radio system for backscatter sensor networks," *IEEE Trans. Wireless Commun.*, vol. 7, no. 6, pp. 2170–2179, Jun. 2008.

[11] S. Kim, C. Mariotti, F. Alimenti, P. Mezzanotte, A. Georgiadis, A. Collado, L. Roselli, and M. M. Tentzeris, "No battery required: perpetual RFID-enabled wireless sensors for cognitive intelligence applications," *IEEE Microw. Mag.*, vol. 14, no. 5, pp. 66–77, Jul. 2013.

[12] S. D. Assimonis, S.-N. Daskalakis, and A. Bletsas, "Sensitive and efficient RF harvesting supply for batteryless backscatter sensor networks," *IEEE Trans. Microw. Theory Techn.*, vol. 64, no. 4, pp. 1327–1338, Apr. 2016.

[13] J. Kimionis and M. M. Tentzeris, "RF tag front-end design for uncompromised communication and harvesting," in *Proc. IEEE Conf. on RFID Techn. and Appl. (RFID-TA)*, Tampere, Finland, Sep. 2014, pp. 109–114.

[14] S. D. Assimonis and A. Bletsas, "Energy harvesting with a low-cost and high efficiency rectenna for low-power input," in *Proc. IEEE Radio and Wireless Symp. (RWS)*, Newport Beach CA, USA, Jan. 2014, pp. 229–231.

[15] S. D. Assimonis, S.-N. Daskalakis, and A. Bletsas, "Efficient RF harvesting for low-power input with low-cost lossy substrate rectenna grid," in *Proc. IEEE Conf. on RFID Techn. and Appl. (RFID-TA)*, Tampere, Finland, Sep. 2014, pp. 1–6.

[16] K. Niotaki, F. Giuppi, A. Georgiadis, and A. Collado, "Solar/EM energy harvester for autonomous operation of a monitoring sensor platform," *Wireless Power Transfer*, vol. 1, no. 01, pp. 44–50, Mar. 2014.

[17] S. Caizzone, E. Digiampaolo, and G. Marrocco, "Investigation of suitable parameters for setup-independent RFID sensing," in *Proc. IEEE Int. EURASIP Workshop on RFID Techn. (EURFID)*, Rosenheim, Germany, Oct. 2015, pp. 98–102.

[18] C. Occhiuzzi, C. Paggi, and G. Marrocco, "Passive RFID strain-sensor based on meander-line antennas," *IEEE Antennas Propagat. Mag.*, vol. 59, no. 12, pp. 4836–4840, Dec. 2011.

[19] R. Nair, E. Perret, S. Tedjini, and T. Barron, "A humidity sensor for passive chipless RFID applications," in *Proc. IEEE Conf. on RFID Techn. and Appl. (RFID-TA)*, Nice, France, Sep. 2012, pp. 29–33.

[20] R. Nair, E. Perret, and S. Tedjini, "Chipless RFID based on group delay encoding," in *Proc. IEEE Conf. on RFID Techn. and Appl. (RFID-TA)*, Sitges, Spain, Sep. 2011, pp. 214–218.

[21] S.-N. Daskalakis, S. D. Assimonis, E. Kampianakis, and A. Bletsas, "Soil moisture wireless sensing with analog scatter radio, low power, ultra-low cost and extended communication ranges," in *Proc. IEEE Sensors Conf.*, Valencia, Spain, Nov. 2014, pp. 122–125.

[22] A. Bletsas, S. Siachalou, and J. Sahalos, "Anti-collision tags for backscatter sensor networks," in *Proc. IEEE 38th Europ. Microw. Conf. (EuMC)*, Amsterdam, Netherlands, Oct. 2008, pp. 179–182.

[23] H. Stockman, "Communication by means of reflected power," *Proc. IEEE IRE*, pp. 1196–1204, Oct. 1948.

[24] K. Kurokawa, "Power waves and the scattering matrix," *IEEE Trans. Microw. Theory Techn.*, vol. 13, no. 2, pp. 194–202, Mar. 1965.

[25] P. V. Nikitin, K. S. Rao, S. F. Lam, V. Pillai, R. Martinez, and H. Heinrich, "Power reflection coefficient analysis for complex impedances in RFID tag design," *IEEE Trans. Microw. Theory Techn.*, vol. 53, no. 9, pp. 2721–2725, Sep. 2005.

[26] J. D. Griffin and G. D. Durgin, "Complete link budgets for backscatter-radio and RFID systems," *IEEE Antennas Propagat. Mag.*, vol. 51, no. 2, pp. 11–25, Apr. 2009.

[27] A. Bletsas, A. G. Dimitriou, and J. N. Sahalos, "Improving backscatter radio tag efficiency," *IEEE Trans. Microw. Theory Techn.*, vol. 58, no. 6, pp. 1502–1509, Jun. 2010.

[28] S. D. Assimonis, E. Kampianakis, and A. Bletsas, "Microwave analysis and experimentation for improved backscatter radio," in *Proc. IEEE Europ. Conf. on Ant. and Prop. (EuCAP)*, Hague, Netherlands, Apr. 2014, pp. 3228–3229.

[29] S. Naderiparizi, A. N. Parks, Z. Kapetanovic, B. Ransford, and J. R. Smith, "Wispcam: A battery-free RFID camera," in *Proc. IEEE Int. Conf. on RFID*, San Diego CA, USA, Apr. 2015.

[30] Y. Zhao and J. R. Smith, "A battery-free RFID-based indoor acoustic localization platform," in *Proc. IEEE Int. Conf. on RFID*, Penang, Malaysia, Apr.–May 2013, pp. 110–117.

[31] A. Dementyev and J. R. Smith, "A wearable UHF RFID-based EEG system," in *Proc. IEEE Int. Conf. on RFID*, Penang, Malaysia, Apr.–May 2013, pp. 1–7.

[32] E. Kampianakis, J. Kimionis, K. Tountas, C. Konstantopoulos, E. Koutroulis, and A. Bletsas, "Wireless environmental sensor networking with analog scatter radio and timer principles," *IEEE Sensors J.*, vol. 14, no. 10, pp. 3365–3376, Oct. 2014.

[33] G. Vannucci, A. Bletsas, and D. Leigh, "Implementing backscatter radio for wireless sensor networks," in *Proc. IEEE Int. Symp. on Person. Indoor and Mob. Radio Commun.*, Athens, Greece, Sep. 2007, pp. 1–5.

[34] J. Kimionis, A. Bletsas, and J. N. Sahalos, "Bistatic backscatter radio for tag read-range extension," in *Proc. IEEE Conf. on RFID Techn. and Appl. (RFID-TA)*, Nice, France, Nov. 2012, pp. 356–361.

[35] "ERC Rep. 25 (2015)." [Online]. Available: http://www.erodocdb.dk/docs/doc98/official/pdf/ERCRep025.pdf

[36] *Custom Silicon Solutions (2009)*, CSS555 micropower timer, Product manual. [Online]. Available: http://www.customsiliconsolutions.com/downloads/Revised%20Standard%20products/CSS555_Spec.pdf

[37] S. W. Smith, *The scientist and engineer's guide to digital signal processing.*, California Technical Publishing, San Diego, 1997.

[38] *Analog Devices (2005)*, ADG902 RF switch, Product manual. [Online]. Available: http://www.analog.com/media/en/technical-documentation/data-sheets/ADG901_902.pdf

[39] *Texas Instruments (2014)*, REF3318 voltage reference IC, Product manual. [Online]. Available: http://www.ti.com/lit/ds/symlink/ref3318.pdf

[40] *Perpetuum Inc. (2010)*, Free-Standing Vibration Energy Harvester. [Online]. Available: http://www.perpetuum.com/fsh.asp

[41] *MicroPelt Inc. (2002)*, MPG-D651 Thermogenerator, Product manual. [Online]. Available: http://thermalforce.de/engl/product/thermogenerator/micropelt_d751.pdf

[42] K. Pohlmann, *Principles of Digital Audio (2nd Edition).*, McGraw-Hill Companies, Inc., 1989.

[43] P. Stoica and R. Moses, *Spectral Analysis of Signals.*, Prentice-Hall International, Inc., 2005.

[44] G. B. Bonan, *Ecological climatology: Concepts and Applications, (1st edition).*, Cambridge Univ. Press, 2002.

[45] J. Kimionis, A. Bletsas, and J. N. Sahalos, "Increased range bistatic scatter radio," *IEEE Trans. Commun.*, vol. 62, no. 3, pp. 1091–1104, Mar. 2014.

[46] N. Fasarakis-Hilliard, P. Alevizos, and A. Bletsas, "Coherent detection and channel coding for bistatic scatter radio sensor networking," *IEEE Trans. Commun.*, vol. 63, no. 5, pp. 1798–1810, May 2015.

[47] P. N. Alevizos and A. Bletsas, "Noncoherent composite hypothesis testing receivers for extended range bistatic scatter radio WSNs," in *Proc. IEEE Int. Conf. on Commun. (ICC)*, London, UK, Jun. 2015, pp. 4448–4453.

[48] S. Kim, R. Vyas, J. Bito, K. Niotaki, A. Collado, A. Georgiadis, and M. M. Tentzeris, "Ambient RF energy-harvesting technologies for self-sustainable standalone wireless sensor platforms," *Proc. IEEE*, vol. 102, no. 11, pp. 1649–1666, Nov. 2014.

[49] F. Lin, Y.-C. Kuo, J.-W. Hsieh, H.-Y. Tsai, Y. Liao, and H. Lee, "A self-powering wireless environment monitoring system using soil energy," *IEEE Sensors J.*, vol. 15, no. 7, pp. 3751–3758, Jul. 2015.

[50] *Instruments, Texas (2011)*, BQ25504 Ultra Low Power Boost Converter with Battery Management. [Online]. Available: http://www.ti.com/lit/ds/symlink/bq25504.pdf

[51] M. Piñuela, P. D. Mitcheson, and S. Lucyszyn, "Ambient RF energy harvesting in urban and semi-urban environments," *IEEE Trans. Microw. Theory Techn.*, vol. 61, no. 7, pp. 2715–2726, Jul. 2013.